

**MANIPULATION OF MAGNETIC VORTEX CORES IN  
PLANAR MAGNETIC MATERIALS USING A VOLTAGE  
INDUCED STRAIN**

**Irene Azaceta**

MSc by Research

University of York

Physics

December 2017

# Abstract

The present work studies the effects of inducing a strain gradient on micron-sized Galfenol and nickel devices containing vortex cores by means of a piezoelectric element. Micromagnetic simulations show that the strain induced anisotropy gradient causes vortex core translation along the direction of the gradient, which is key to efficient excitation of the core dynamics. The effect of the strain gradient symmetry on the displacement of the core is investigated and the experimental implementation of the strain gradient is also discussed. For the latter, two approaches are considered. The first is to make use of the ferroelastic multi-domain state of a ferroelectric substrate. The second is based on tailoring a gradient in the strain by patterning two electrodes on top of the piezoelectric substrate.

# Contents

<b>Abstract</b>	<b>2</b>
<b>List of contents</b>	<b>3</b>
<b>Acknowledgements</b>	<b>5</b>
<b>Declaration</b>	<b>6</b>
<b>1 Introduction</b>	<b>7</b>
<b>2 Background</b>	<b>9</b>
2.1 Energy contributions of ferromagnetism . . . . .	9
2.1.1 The exchange energy . . . . .	9
2.1.2 The magnetocrystalline anisotropy . . . . .	11
2.1.3 The magnetostatic energy and shape anisotropy . . . . .	13
2.1.4 The magnetoelastic energy . . . . .	15
2.1.5 The Zeeman energy . . . . .	16
2.2 Micromagnetics . . . . .	16
2.3 Magnetic vortices in planar magnetic materials . . . . .	18
2.3.1 Introduction to the magnetic vortex state . . . . .	18
2.3.2 Dynamical properties of the magnetic vortex . . . . .	19
2.4 Multiferroic materials and magnetoelectricity . . . . .	21
2.5 Voltage driven manipulation of magnetic vortices . . . . .	23
<b>3 Method</b>	<b>27</b>
3.1 Micromagnetic simulations . . . . .	27
3.2 Design of the samples . . . . .	29
3.3 Experimental techniques . . . . .	31

3.3.1	Fabrication techniques . . . . .	31
3.3.1.1	Thermal evaporation . . . . .	31
3.3.1.2	Electron Beam Lithography (EBL) . . . . .	33
3.3.1.3	Demagnetization routine . . . . .	34
3.3.2	Imaging techniques . . . . .	35
3.3.2.1	X-Ray Magnetic Circular Dichroism (XMCD) . . . . .	35
3.3.2.2	X-Ray Photoemission Electron Microscopy (X-PEEM) . . . . .	37
3.3.2.3	Magnetic force microscopy (MFM) . . . . .	38
<b>4</b>	<b>Results</b>	<b>43</b>
4.1	Micromagnetic simulations . . . . .	43
4.1.1	Effects of an anisotropy gradient on a Galfenol element . . . . .	44
4.1.2	Effects of an anisotropy gradient on a nickel element . . . . .	49
4.2	Experimental results . . . . .	53
4.2.1	Experiment E1 . . . . .	53
4.2.2	Experiments E2 and E3 . . . . .	57
<b>5</b>	<b>Conclusions and outlook</b>	<b>62</b>
	<b>Bibliography</b>	<b>64</b>

# Acknowledgements

First of all, I would like to thank my supervisor Dr. Stuart Cavill for giving me the fantastic opportunity to carry out this project as part of his group at the University of York, as well as for all his guidance and advice throughout the process.

I would also like to express my gratitude to Dr. Chris Reardon for all those times at the cleanroom helping me with the thermal evaporator and the electron beam system. This work could not have been done either without the aid of Dr. Andrew Rushforth and his team who deposited the ferromagnetic material for us. Thanks to Daan Arroo for such a great training on the MFM at Imperial College London, where I learnt most of the tricks that I needed to finally success with the Bioscope Resolve at York. To my groupmates Chris and James, thank you both for helping me in the lab and for sharing your knowledge with me.

I am grateful also to my friends from the nuclear group David and Mei for all the nice times that we spent at the common room, which made the journey much more enjoyable. I could not imagine doing this master without Antonio, who suffered all my complains about the MFM and who gave me all the emotional support that I needed to get through the hard times.

To my good friend Amy, thanks for all your craziness and for being always there. Noski, ezin naiz nire betiko lagun minenaz ahaztu ere egin. Clau, Garbi eta Itzi eskerrik asko nahiz eta urrun izan, oso gertu sentitu izan zaituztedalako beti.

Finalmente, quiero agradecer con todo mi cariño a mis padres y a Jon por hacer posible este máster y prestarme todo el apoyo que he necesitado durante este viaje.

# Declaration

I declare that this thesis is a presentation of original work and I am the sole author. This work has not previously been presented for an award at this, or any other, University. All sources are acknowledged as References.

# Chapter 1

## Introduction

The great variety of structures and properties found in magnetic systems makes these very useful for several technological and biomedical applications. Advances in such applications require further device miniaturization, which has focused the attention of scientists on the ability of controlling magnetism in reduced dimensions, for example magnetic surfaces, interfaces, thin films, micro- and nano-scale structures and nanoparticles. Progress in microfabrication technology has enabled the preparation of a variety of magnetic structures which have eventually arisen as promising candidates for ultrahigh density data storage, magnetic random-access memories (MRAM), magnetic field nanosensors and spintronic logic devices. In 2D magnetic systems, topological defects such as Skyrmions [1] and magnetic vortices [2] are of particular interest. The magnetic vortex structure is being investigated thoroughly mainly because of its intriguing dynamical properties, especially the appearance of a gyrotropic mode at sub-GHz frequencies. Such a low-frequency mode refers to the spiral, circular if no damping, motion of the vortex core when it is displaced from its equilibrium position and is key for applications in data recording and oscillators.

Magnetic vortices have been discussed heavily as possible bit elements in MRAM due to their high stability with respect to static external magnetic fields [3, 4, 5] and to the low stray fields present in these textures. This allows vortices to be packed more closely than usual single domain states providing a pathway to a high density magnetic storage device. The utilization of the magnetic vortex as a bit element is based on regarding the two possible states of either its polarity or its chirality as the two bits of information “0” and “1”. Combining both properties, the magnetic vortex is a promising candidate for a

four state memory device [6]. Also, given the gyrotropic mode, it has been considered as a potential microwave source in spin torque vortex oscillators (STVO-s) [7].

Excitation of vortex core motion is not only essential for microwave emission but has been shown to provide a means to switch the polarity and chirality of the soliton itself, allowing for data writing in magnetic memory applications. Dynamic in-plane perturbations of very low amplitude induce polarity switching at subnanosecond scales when the gyrotropic mode is excited resonantly. These perturbations include magnetic field pulses [8, 9, 10], oscillating fields [11, 12, 13, 14], spin currents [15] and RF strain gradients [16]. With respect to chirality, a gyromode-mediated control of the spin circulation has also been found achievable when in-plane nanosecond field pulses are applied to asymmetric structures [17].

The desire for reducing power consumption led years ago to the quest of another way for controlling magnetization other than magnetic fields. Magnetoelectrics, which refers to the manipulation of magnetization using electric fields or voltages emerged as a promising answer to this, which on top, allows addressing magnetic elements individually due to the much reduced stray field. In this context, there has been a recent interest in using electric voltage induced strain to control magnetization in composites consisting of a piezoelectric (PE) or ferroelectric (FE) substrate and a magnetostrictive ferromagnetic (FM) element. The manipulation of magnetic textures containing vortices by the application of strain has been reported in Galfenol ( $\text{Fe}_{81}\text{Ga}_{19}$ ) [18] and nickel (Ni) [19] where the strain acts as an additional uniaxial anisotropy. In contrast to a spatially uniform uniaxial strain, which does not displace the vortex core [18], a 1-D linear strain gradient has been found to induce vortex core dynamics [16]. In this work, the effect of the strain gradient symmetry on the displacement of the vortex core is investigated in  $\text{Fe}_{81}\text{Ga}_{19}/\text{PE-FE}$  and  $\text{Ni}/\text{PE-FE}$  composites as it is relevant for efficient excitation of the core dynamics.

# Chapter 2

## Background

### 2.1 Energy contributions of ferromagnetism

Magnetism is a purely quantum mechanical effect that occurs when atoms with unpaired electrons, and therefore with a non-zero net magnetic moment  $\vec{\mu}$ , are arranged in a crystal lattice. If the magnetic moments interact sufficiently strongly with each other, ferromagnetism occurs. The magnetic free energy of a ferromagnetic system is defined by four interactions: the exchange coupling, the spin-orbit coupling, the magnetostatic interaction and the Zeeman interaction. These interactions give rise to different energy terms that will be introduced below.

#### 2.1.1 The exchange energy

The origin of ferromagnetism relies on the exchange coupling. This is a quantum mechanical effect that arises from the combination of Pauli's exclusion principle and the Coulomb interaction, involving only spin degrees of freedom. In a two electron system, the orbital part of the wave function of the joint state,  $\Phi$ , is built from the product of the two single electron states,  $\phi_a$  and  $\phi_b$ , in such way that the exchange symmetry between the two electrons is obeyed. This leads to two possible orbital wave functions for the system, one of which is symmetric and the other antisymmetric:

$$\begin{aligned}\Phi_T &\propto [\phi_a(\vec{r}_1)\phi_b(\vec{r}_2) + \phi_b(\vec{r}_1)\phi_a(\vec{r}_2)] && \text{symmetric} \\ \Phi_S &\propto [\phi_a(\vec{r}_1)\phi_b(\vec{r}_2) - \phi_b(\vec{r}_1)\phi_a(\vec{r}_2)] && \text{antisymmetric}\end{aligned}\tag{2.1}$$

Electrons have been labelled as 1 and 2. Taking into account the electrostatic repulsion, the two orbital states above are not degenerate, and the energy difference between them is known as the exchange energy. Even if the origin of the exchange interaction is the energy dependence on the orbital symmetry, Pauli's symmetry requirement over the complete wave function, which includes both orbital and spin parts, results in the correlation between the orbital symmetry and the spin alignment. Consequently, it is possible to express the exchange coupling as an effective spin-spin interaction, specifically, the scalar product of the two electron spins, such that:

$$E_{exch}^{el} = -2J\hat{S}_1 \cdot \hat{S}_2 \quad (2.2)$$

$\hat{S}_1$  and  $\hat{S}_2$  are the spin operators of electron 1 and 2 respectively, and  $J$  is known as the exchange coupling strength or simply, as the exchange parameter. In this notation, spin operators are dimensionless and the exchange parameter has units of energy. In a solid, where the electronic wave functions of nearby atoms overlap, the exchange coupling is generalized as a pair-wise spin interaction known as the Heisenberg model:

$$E_{exch} = -\sum_{i,j} J_{ij}\hat{S}_i \cdot \hat{S}_j \quad (2.3)$$

Here,  $J_{ij}$  is the exchange parameter between two interacting spins  $i$  and  $j$  in the lattice. Assuming only interactions between nearest neighbours and an isotropic exchange, the expression above is simplified to:

$$E_{exch} = -J \sum_{\langle i,j \rangle} \hat{S}_i \cdot \hat{S}_j \quad (2.4)$$

For a ferromagnet  $J > 0$  and the exchange coupling favours the spins, and hence the magnetic moments, to be aligned in the crystal lattice, leading to a non-vanishing value of the magnetization even at zero magnetic field. For an antiferromagnet  $J < 0$  and it becomes energetically favourable for neighbouring spins to point in opposite directions.

The exchange coupling is a short range force. In ferromagnetic materials, the coexistence of short range forces and long range forces such as the magnetostatic interaction, makes it difficult to describe their macroscopic magnetic behaviour. A method to overcome

this issue is to replace the atomic nature of the matter and the quantum mechanical interactions by a continuum model.

In this approach, the magnetization is considered to be a continuous field  $\vec{M}(\vec{r})$ , where  $\vec{r}$  is the position vector in the ferromagnetic body. The magnitude of the magnetization is assumed to be constant and equal to the saturation magnetization,  $M_s$ , and only its orientation varies throughout the system. That is,  $\vec{M}(\vec{r}) = M_s \vec{m}(\vec{r})$ , where  $\vec{m}$  is a dimensionless unit vector known as the reduced magnetization and  $M_s$  has units of  $A/m$ . In this context, it is necessary to find a continuum expression for the exchange energy. Considering the spin operators in (2.4) as classical vectors, for a crystal of uniform spins,  $|\vec{S}_i| = S$ , the exchange energy density<sup>1</sup> in the continuum approximation becomes:

$$U_{exch} = A |\nabla \vec{m}(\vec{r})|^2 \quad (2.5)$$

The integral extends over the volume of the body.  $A$  is called the exchange stiffness and has units of energy per unit length. It is related to  $J$  as:

$$A = \frac{JS^2}{a} C \quad (2.6)$$

where  $a$  is the nearest neighbour distance and  $C$  is the number of sites in the unit cell.

### 2.1.2 The magnetocrystalline anisotropy

Even if the exchange coupling manages to explain the alignment of the spins and ultimately, the magnetic moments in a ferromagnet, it only gives information on the relative orientation of the spins. There are several contributions to the anisotropy of the system that will eventually define the preferential crystallographic orientations along which the magnetic moments align. One of the main sources of anisotropy is the magnetocrystalline anisotropy, which refers to the coupling between the lattice symmetry and the magnetic configuration of the system.

The origin of the magnetocrystalline anisotropy is the combination of the spin-orbit coupling and the crystal fields. The spin-orbit interaction couples the spin angular momentum and the orbital angular momentum of an electron. It arises from the

---

<sup>1</sup>In this work, energies,  $E$ , are distinguished from energy densities,  $U$ .

electromagnetic interaction between the electron spin and the magnetic field generated by the same electron orbiting around the nucleus. Given a certain ion in the crystal, all the neighbouring ions produce an electric field called the crystal field, which generates attractive or repulsive forces on the first ion. Depending on the crystal symmetry, the orbitals must arrange differently so that the electrostatic repulsion is minimized. Due to the spin-orbit coupling, such orbital orientations cause certain spin orientations to be energetically favourable. These are known as easy axes.

The symmetry of the magnetocrystalline anisotropy is the same as that of the crystal lattice. Consequently, a cubic crystal as nickel (Ni) or Galfenol ( $\text{Fe}_{81}\text{Ga}_{19}$ ) has a cubic anisotropy with 3 easy axes. The corresponding energy density can be expressed as a series expansion of the direction cosines  $\alpha_1$ ,  $\alpha_2$  and  $\alpha_3$  between the magnetization and the principal crystallographic axes  $\vec{u}_1 = [100]$ ,  $\vec{u}_2 = [010]$  and  $\vec{u}_3 = [001]$ :

$$U_{can} = K_{c0} + K_{c1} (\alpha_1^2 \alpha_2^2 + \alpha_2^2 \alpha_3^2 + \alpha_3^2 \alpha_1^2) + K_{c2} \alpha_1^2 \alpha_2^2 \alpha_3^2 + \dots \quad (2.7)$$

$K_{c0}$ ,  $K_{c1}$ ,  $K_{c2}$  ... are called anisotropy coefficients and have units of energy per unit volume. As  $K_{c0}$  has no directional dependence, the first coefficient is the most relevant and the expression can be simplified to:

$$U_{can} = K_c (\alpha_1^2 \alpha_2^2 + \alpha_2^2 \alpha_3^2 + \alpha_3^2 \alpha_1^2) \quad (2.8)$$

with  $K_{c1} = K_c$ .

In hexagonal crystals as cobalt, the crystal symmetry causes a uniaxial anisotropy with a single easy axis. The easy axis coincides with  $\vec{u}_3$  and any direction in the basal plane is an equally hard direction along which a much larger field is required to magnetize the body. The mathematical expression for the uniaxial anisotropy is a series of powers of the direction cosines weighted by the corresponding anisotropy coefficients:

$$U_{uan} = K_{u0} + K_{u1} \alpha_3^2 + K_{u2} \alpha_3^4 + \dots \quad (2.9)$$

Again, discarding the 0<sup>th</sup> order element and neglecting 2<sup>nd</sup> and higher order contributions:

$$U_{uan} = K_u \alpha_3^2 \quad (2.10)$$

with  $K_{u1} = K_u$ . Written in terms of the reduced magnetization:

$$U_{uan} = K_u (\vec{m} \cdot \vec{u}) \quad (2.11)$$

where  $\vec{u}_3 = \vec{u}$ .

### 2.1.3 The magnetostatic energy and shape anisotropy

The magnetostatic interaction refers to the interaction between the magnetic field generated by the magnetic distribution of the system and the magnetization itself. In a ferromagnet, each magnetic dipole, which is represented by the magnetic moment  $\vec{\mu}_j$ , produces a magnetic field  $\vec{h}^j$  centered at the atomic position  $\vec{r}_j$  that extends all over the space:

$$\vec{h}^j = \frac{1}{4\pi} \left[ -\frac{\vec{\mu}_j}{|\vec{r} + \vec{r}_j|^3} + \frac{3}{|\vec{r} - \vec{r}_j|^5} [\vec{\mu}_j \cdot (\vec{r} - \vec{r}_j)] (\vec{r} - \vec{r}_j) \right] \quad (2.12)$$

As a consequence, a dipole in the  $i^{\text{th}}$  lattice point  $\vec{\mu}_i$ , interacts with the dipolar field created by the rest of the dipoles. The energy of  $\vec{\mu}_i$  is then:

$$E_i = -\vec{\mu}_i \cdot \sum_{j \neq i} \mu_0 \vec{h}^j \quad (2.13)$$

Summing all the individual contributions, the magnetostatic energy can be expressed as:

$$E_{ms} = - \sum_i \vec{\mu}_i \cdot \sum_{j \neq i} \mu_0 \vec{h}^j \quad (2.14)$$

It is usual to write (2.14) as a function of the total dipolar field, known as the magnetostatic field, which is the sum of the individual fields (2.12) generated by all the dipoles in the crystal:

$$E_{ms} = -\frac{\mu_0}{2} \sum_i \vec{\mu}_i \vec{H}_d \quad (2.15)$$

with  $H_d = \sum_j \vec{h}^j$ . The magnetostatic field is usually called the *demagnetizing field* inside the body and the *stray field* outside the body. In the continuum approximation, it can be approximated to:

$$\vec{H}_d = \frac{1}{4\pi} \left[ \int_V \frac{\rho_v(\vec{r}')(\vec{r}-\vec{r}')}{|\vec{r}-\vec{r}'|^3} dV + \int_s \frac{\rho_s(\vec{r}')(\vec{r}-\vec{r}')}{|\vec{r}-\vec{r}'|^3} dS \right] \quad (2.16)$$

where  $\rho_v$  and  $\rho_s$  stand for the volume and the surface magnetic charge density respectively. This finally leads to the continuum expression of (2.15):

$$U_{ms} = -\frac{\mu_0 M_s}{2} \vec{m} \cdot \vec{H}_d \quad (2.17)$$

For particular geometries as ellipsoids or spheres, the demagnetizing field is uniform and can be written as:

$$\vec{H}_d = -M_s \overline{\overline{N}} \vec{m} \quad (2.18)$$

where  $\overline{\overline{N}}$  is the so-called demagnetizing tensor.

When the ferromagnetic body is uniformly magnetized, the first integrand of equation (2.16) is zero. In that case, the magnetostatic energy only depends on the shape of the body and the direction of the magnetization, and has the same mathematical form as the uniaxial anisotropy. Then, the dipolar energy is usually referred to as *shape anisotropy*. In thin films, the shape anisotropy tends to keep the magnetization within the film plane.

In a structure small enough, the single-domain configuration is energetically favourable. In that case, the cost generated by the demagnetizing fields inside the body is compensated by the minimization of the exchange energy. However, in larger systems, the increase in the magnetostatic energy cannot be compensated any more and consequently, the body splits into several magnetic domains. That way, the magnetostatic energy is minimized.

The formation of domains occurs in spite of an increase in the exchange energy at the

domain walls, where there is a gradual rotation of spins. This occurs over lengths of the order of tens to hundreds of nanometers leading to *Bloch* or *Néel* type domain walls.

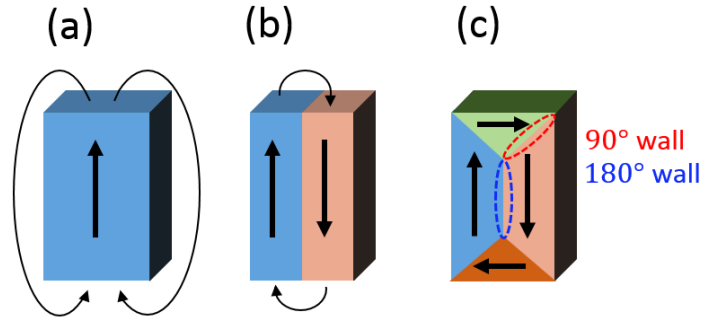


Figure 2.1: Formation of magnetic domains in order to minimize the dipolar contribution. (a) corresponds to a single-domain state. Here, the exchange energy is minimum but the dipolar energy is the largest due to the big dipolar fields. In (b) the system splits into two domains reducing the magnetostatic contribution at the expense of creating a domain wall. Finally, in (c) the demagnetizing fields are cancelled minimizing the dipolar energy but introducing several domain walls. The resulting 4-domain configuration is known as the flux-closure or Landau structure.

#### 2.1.4 The magnetoelastic energy

The magnetoelastic interaction or magnetostriction stands for the coupling between the magnetization of the body and the strain applied to it. Essentially, if a strain is applied, the distances between atoms change and the lattice is distorted. As a consequence, the crystal fields change and the spin configuration of the system is modified. The magnetoelastic energy is a function of the direction cosines of the magnetization and the components  $\epsilon_{ij}$  of the strain tensor. For a cubic crystal:

$$U_{me} = B_1 (\alpha_1^2 \epsilon_{xx} + \alpha_2^2 \epsilon_{yy} + \alpha_3^2 \epsilon_{zz}) + B_2 (\alpha_1 \alpha_2 \epsilon_{xy} + \alpha_2 \alpha_3 \epsilon_{yz} + \alpha_3 \alpha_1 \epsilon_{zx}) \quad (2.19)$$

where  $B_1$  and  $B_2$  are the so-called magnetoelastic coupling constants in J/m, which depend on the elastic moduli  $C_{11}$ ,  $C_{21}$  and  $C_{44}$ , and the magnetostriction constants  $\lambda_{100}$  and  $\lambda_{111}$ :

$$B_1 = -\frac{3}{2} \lambda_{100} (C_{11} - C_{12})$$

$$B_2 = 3C_{44} \lambda_{111} \quad (2.20)$$

If the magnetization is restricted to be in-plane ( $\alpha_3 = 0$ ) and negligible in-plane shear strain is assumed ( $\epsilon_{xy} = 0$ ), the expression can be simplified to:

$$U_{me} = B_1 \alpha_1^2 (\epsilon_{xx} - \epsilon_{yy}) = B_1 \Delta\epsilon \cos^2 \phi \quad (2.21)$$

where  $\phi$  denotes the angle between the magnetization and the [100] direction, and  $\Delta\epsilon = \epsilon_{xx} - \epsilon_{yy}$  is the in-plane strain anisotropy. Comparing equation (2.21) to the expression for the magnetocrystalline uniaxial anisotropy (2.10), one can see that the magnetoelastic energy above is another type of uniaxial anisotropy with  $K_u = K_s = B_1 \Delta\epsilon$ .

### 2.1.5 The Zeeman energy

Finally, if an external magnetic field is applied to the ferromagnetic system, the magnetic moments inside the body tend to align with the external field. The energy term that describes this effect is the Zeeman term, which is given by:

$$U_z = -\mu_0 M_s \vec{m} \cdot \vec{H}_{ext} \quad (2.22)$$

where the magnetic field is in A/m units.

## 2.2 Micromagnetics

The micromagnetic formulation seeks the description and prediction of magnetic behaviours at micro- and nano-length scales. In this model, the magnetization is represented by a continuous field of constant magnitude. In micromagnetics two approaches are distinguished, the static approach and the dynamic approach.

On the one hand, the static approach minimizes the energy of the body with respect to the spatial distribution of the magnetization,  $\vec{m}(\vec{r})$ , to calculate equilibrium magnetic configurations. Taking into account all the energy contributions in § 2.1, the total energy of a cubic ferromagnet with in-plane magnetization is given by:

$$E = \int_V \left[ A(\nabla \vec{m})^2 + K_c(\alpha_1^2 \alpha_2^2 + \alpha_2^2 \alpha_3^2 + \alpha_3^2 \alpha_1^2) - \frac{\mu_0 M_s}{2} \vec{m} \cdot \vec{H}_d + B_1 \Delta \epsilon \cos^2 \phi - \mu_0 M_s \vec{m} \cdot \vec{H}_{ext} \right] dV \quad (2.23)$$

By using variational principles, it can be shown that the energy minimum satisfies the following condition:

$$\vec{m} \times \vec{H}_{eff} = 0 \quad (2.24)$$

where  $\vec{H}_{eff}$  is a local effective field that involves all the interactions described:

$$\vec{H}_{eff}(\vec{r}) = -\frac{\partial E}{\partial \vec{m}(\vec{r})} \quad (2.25)$$

That is, the equilibrium is reached when  $\vec{m}(\vec{r})$  aligns to the local effective field at  $\vec{r}$ .

On the other hand, the dynamical approach looks for the time evolution of the magnetization. An equation that describes the time dependence of the magnetization was presented by Landau and Lifshitz in 1935 [20]. It is known that an external magnetic field causes the precession of the magnetic moment around it, the so-called Larmor precession. Landau and Lifshitz suggested that the magnetization  $\vec{m}(\vec{r})$  also precesses due to the local effective field:

$$\frac{d\vec{m}}{dt} = -\gamma \vec{m} \times \vec{H}_{eff} \quad (2.26)$$

where  $\gamma = \frac{gq_e}{2m_e}$  is the gyromagnetic ratio with  $g$  the Landé factor. To take into consideration dissipative effects, which cause the magnetization in actual systems to slow down and eventually stop, a damping term was introduced. This led to the Landau-Lifshitz-Gilbert (LLG) differential equation:

$$\frac{d\vec{m}}{dt} = -\gamma \left( \vec{m} \times \vec{H}_{eff} - \eta \frac{\vec{m} \times d\vec{m}}{dt} \right) \quad (2.27)$$

The first term in (2.27) represents the torque exerted by the effective field. The second term is the damping term, governed by damping parameter  $\eta$ . By integrating the

LLG equation the evolution of the magnetization is obtained until at equilibrium, the magnetization and the effective field are parallel.

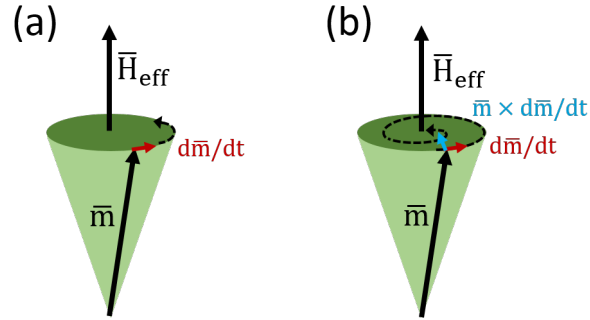


Figure 2.2: Undamped (a) and damped (b) motion of the magnetization vector around the effective field  $\vec{H}_{eff}$  representing equations (2.26) and (2.27) respectively.

## 2.3 Magnetic vortices in planar magnetic materials

### 2.3.1 Introduction to the magnetic vortex state

Lateral confinement in some planar magnetic materials leads to a magnetic vortex configuration. The topological defect is observed in square and circular geometries of micron and sub-micron dimensions in soft ferromagnetic materials such as Permalloy ( $\text{Fe}_{80}\text{Ni}_{20}$ ) [21]. In these elements the vortex state arises as a result of the balance between the exchange energy and the magnetostatic energy and is characterized by an in-plane magnetization everywhere in the element except at the centre, where the magnetization rotates out of plane. Such a central region is known as the vortex core and has a diameter of about 20 nm.

In square elements, the in-plane magnetization forms a Landau closed flux [22] as shown in Fig.2.3 (a). The square is divided into 4 magnetic domains and the magnetization in each domain forms an angle of  $90^\circ$  with that of the two neighbours. This manages to cancel any stray fields and therefore, minimizes the magnetostatic energy. However, it increases the exchange energy of the system. In order to avoid a singularity at the centre, the vortex core arises. Similarly, in soft circular structures the magnetic moments curl in the sample plane minimizing the dipolar energy and the increasing angles between adjacent spins force a vortex core formation at the centre, Fig.2.3 (b).

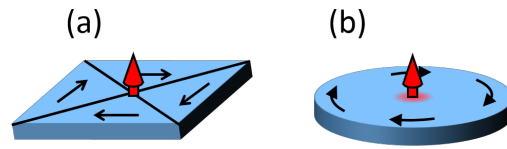


Figure 2.3: Vortex state in dots of different shapes showing an in plane flux-closure configuration.

Polarity ( $P$ ) and chirality ( $C$ ) define the state of the soliton. Polarity specifies the orientation of the magnetization inside the vortex core with respect to the sample plane, whereas chirality indicates the sense of the in-plane magnetization. Both quantities can only take two values,  $+1/-1$ , and therefore, the magnetic vortex has 4 possible states, Fig.2.4.

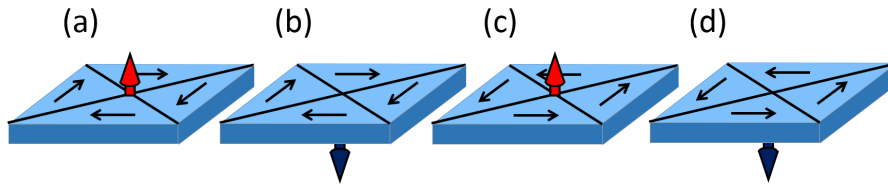


Figure 2.4: Four possible states of the flux closure vortex configuration: (a)  $P=1$  and  $C=1$ ; (b)  $P=-1$  and  $C=1$ ; (c)  $P=1$  and  $C=-1$ ; and (d)  $P=-1$  and  $C=-1$ .

### 2.3.2 Dynamical properties of the magnetic vortex

At non-zero temperature, ferromagnetic order is disrupted by spin fluctuations known as *spin waves*<sup>2</sup>. Spin waves can be classically pictured as coupled precessions of spins around the ordered moment in the ferromagnet. In a normal mode, the spins precess at the same frequency and with a constant phase difference with respect to their neighbours, giving rise to a waveform of frequency  $\omega$  and wave vector  $k$ . Spin waves are quantized as magnons, with an angular momentum of  $1\hbar$  and a magnetic moment of  $1g\mu_B$ . Spin waves can be excited, or equivalently, magnons can be produced, by using dynamic magnetic fields.

In a flux-closed configuration, the spin-wave spectrum includes radial modes and azimuthal modes. When a magnetic vortex is introduced, Fig.2.3, the spectrum is affected so that the degeneracy of the azimuthal modes with opposite rotation sense is shifted [23] and a low frequency sub-GHz mode, the gyrotropic mode, appears [24, 25]. The gyrotropic mode is a translational mode that arises when the core is moved away from

<sup>2</sup>Actually, these fluctuations still exist at  $T = 0$  due to the zero point energy.

its equilibrium position by a perturbation such as an external magnetic field. When the perturbation is turned off, ideally the core would endlessly gyrate in a circular orbit. Actually, due to damping effects, the core goes back to the equilibrium position in a spiral motion. This motion can be described using an alternative form of the LLG equation, which was first introduced by A. Thiele [26]. Assuming that the vortex core moves as a rigid object, (2.27) can be transformed to the following force equation [27]:

$$\vec{F} = \overline{\overline{G}} \cdot \dot{\vec{r}} + \overline{\overline{g}} \cdot \dot{\vec{r}} \quad (2.28)$$

where  $\vec{r} = \vec{r}(x, y)$  is the position of the vortex core in the film. The first term,  $\vec{F}_G = \overline{\overline{G}} \cdot \dot{\vec{r}}$ , is known as the gyroforce and it is responsible for the vortex core oscillation.  $\overline{\overline{G}}$  is the so-called *gyromagnetic tensor*<sup>3</sup> whose components are given by:

$$G_{ij} = \frac{M_s}{\gamma} \int \vec{m} \cdot \left( \frac{\vec{m}}{r_i} \times \frac{\vec{m}}{r_j} \right) d^2r \quad (2.29)$$

The second term,  $\vec{F}_g = \overline{\overline{g}} \cdot \dot{\vec{r}}$ , is the damping force which causes the shifted vortex core to return to equilibrium.  $\overline{\overline{g}}$  is called the *dissipation tensor* and its components are given by:

$$g_{ij} = \eta M_s \int \left( \frac{\vec{m}}{r_i} \cdot \frac{\vec{m}}{r_j} \right) d^2r \quad (2.30)$$

Finally,  $\vec{F}$  corresponds to the remaining forces acting on the vortex, which include restoring forces ( $\vec{F}_r$ ) pointing towards the centre of the sample:

$$\vec{F} = - \frac{\partial E(\vec{r})}{\partial \vec{r}} \quad (2.31)$$

where  $E$  is the free energy of the vortex. A simplified diagram of the forces acting during the gyrotropic motion of an out-of plane vortex core is represented for a 2-dimensional structure in Fig.2.5:

---

<sup>3</sup>The gyromagnetic tensor is usually expressed as the so-called gyrovector ( $\vec{G}$ ) such that  $G_{ij} = \epsilon_{kij} G_k$  with  $\epsilon_{kij}$  the Levi-Civita symbol.

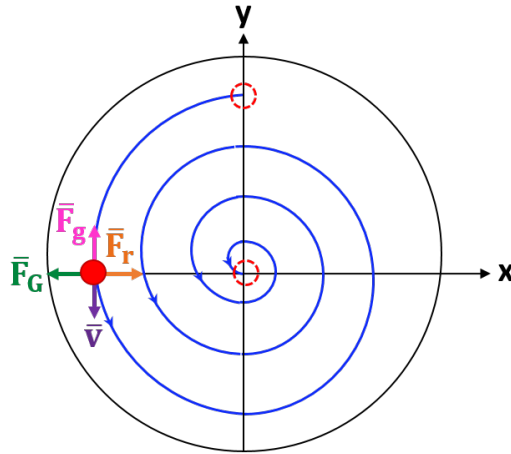


Figure 2.5: Depiction of the forces acting during the gyrotropic motion of the vortex state for a planar ferromagnetic disc. The vortex core (red dot), which points along the  $\hat{z}$  direction, follows a spiral motion when it is displaced from the equilibrium position at the centre of the element.

## 2.4 Multiferroic materials and magnetoelectricity

In the same way ferromagnetic (FM) materials exhibit a spontaneous magnetization at zero magnetic field, ferroelectric (FE) and ferroelastic (FS) materials show a spontaneous polarization and strain respectively, both of which can be reversed by an external electric field. Ferromagnetism, ferroelectricity and ferroelasticity are ferroic properties and by definition, a single-phase multiferroic material is the one that shows two or more of them in the same phase. Magnetoelectricity, on the other hand, is an independent phenomenon that refers to the coupling between the ferromagnetic and the ferroelectric properties of any material with both magnetic and electronic polarizability, regardless of whether it is multiferroic or not.

The ultimate goal for device applications, would be a single-phase multiferroic with a strong coupling between the ferroelectric and ferromagnetic order parameters. That way, electric fields would not only reorient polarization but would allow a simple and more energetically efficient control of the magnetization at room temperature. However, only a very few room temperature single-phase multiferroic materials have been reported. For that reason, in the last decades, the focus of many researches has been to design and identify new mechanisms for a large magnetoelectric coupling and multiferroic behaviour. The latter includes bilayer samples where a thin-film layer of a magnetostrictive ferromagnetic material is grown on a piezoelectric (PE) substrate.

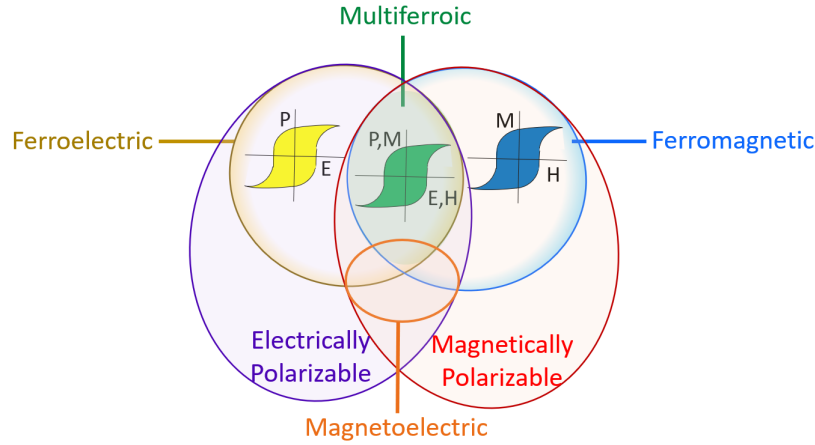


Figure 2.6: Diagram showing the relationship between multiferroic and magnetoelectric materials.

Such composite systems operate by coupling the magnetic and electric properties between the two materials via strain. When an electric field is applied, a strain is generated in the piezoelectric:

$$\epsilon_{ij} = d_{kij}E_k \quad \text{with } i,j,k = 1,2,3 \quad (2.32)$$

Here,  $d_{kij}$  are the components of the third rank piezoelectric tensor and  $E_k$  the components of the electric field. This is usually written in a 2-subscript matrix notation:

$$\epsilon_i = d_{ki}E_k \quad \text{with } k = 1,2,3 \text{ and } i = 1,2,3,4,5,6 \quad (2.33)$$

where the strain is now a 6-component vector

$$\vec{\epsilon} = \begin{bmatrix} \epsilon_1 \\ \epsilon_2 \\ \epsilon_3 \\ \epsilon_4 \\ \epsilon_5 \\ \epsilon_6 \end{bmatrix} = \begin{bmatrix} \epsilon_{xx} \\ \epsilon_{yy} \\ \epsilon_{zz} \\ \epsilon_{yz} \\ \epsilon_{zx} \\ \epsilon_{xy} \end{bmatrix} \quad (2.34)$$

and the piezoelectric tensor is substituted by a  $6 \times 3$  matrix where  $d_{ki}$  is the strain induced in the direction  $i$  per unit electric field applied along  $k$ .

Subsequently, such a strain produces a change in the magnetic anisotropy via the inverse magnetostriction effect. In order to induce large changes in the magnetic configuration through the generation of magnetoelastic anisotropy (2.21), materials with large magnetostriction coefficients are sought. Regarding the piezoelectric substrate,

materials with large piezoelectric coefficients are pursued. Given that piezoelectricity has a similar origin to ferroelectricity (non-centrosymmetry), piezoelectric materials are also ferroelectrics. A good understanding of the ferroelectric properties becomes then essential as they determine the piezoelectric properties themselves, as will be seen in § 2.5.

## 2.5 Voltage driven manipulation of magnetic vortices

As introduced in chapter 1, patterned magnetic nanostructures have been widely investigated for applications in non-volatile data storage and magnetic random-access memories. Searching for a low power writing mechanism, the possibility of switching the magnetization through an electric field induced strain has been extensively studied. For that purpose, the ferromagnetic nanostructures are coupled to a piezoelectric substrate where the strain is generated and transferred to the former. A magnetoelastic anisotropy is then created by magnetostriction effects, which can switch magnetization.

The strain anisotropy  $\Delta\epsilon$  needed to produce the magnetoelastic anisotropy (2.21) can be achieved by using the sign difference between the piezoelectric coefficients  $d_{33}$  and  $d_{31}$  of conventional high piezoelectric ceramic actuators as  $\text{Pb}[\text{Zr}_x\text{Ti}_{1-x}]\text{O}_3$  (PZT) [28]. When a voltage is applied along its dominant elongation axis  $\hat{z}$ , the actuator expands along the latter and contracts along the two orthogonal directions  $\hat{x}$  and  $\hat{y}$  (Fig.2.7). Therefore, if a magnetostrictive film is affixed to the  $\hat{x} - \hat{z}$  face, it exhibits a compressive strain along  $\hat{x}$  and a tensile strain along  $\hat{z}$ .

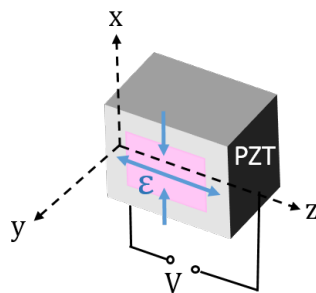


Figure 2.7: Sketch of the response of a magnetostrictive film coupled to a PZT ceramic, to a voltage applied along the dominant elongation axis of the piezoelectric.

Another way of generating an anisotropic strain is to use the (011) cut of single crystal relaxor ferroelectrics as  $(1-x)\text{Pb}(\text{Mg}_{1/3}\text{Nb}_{2/3})\text{O}_3 - x\text{PbTiO}_3$  (PMN-xPT,  $0 < x < 0.35$ ). This ferroelectric has received much attention during the last decade due to its extremely high

piezoelectric response at room temperature, which relates to the fact that it situates very close to the boundary where tetragonal, orthorhombic, rhombohedral and monoclinic phases meet. The (011) cut is particularly suitable because it can produce a large and well-defined uniaxial anisotropy by inducing simultaneously compressive and tensile strains in the orthogonal  $[100]$  ( $\hat{x}$ ) and  $[010]$  ( $\hat{y}$ ) in-plane directions.

The unique properties of the PMN-xPT rely on its crystal structure, orientation and domain states. The (011)-oriented rhombohedral PMN-xPT ( $x = 0.32$ ) has 8 possible polarization directions along the  $\langle 111 \rangle$  variants, represented by the dashed lines in Fig.2.8 (a). When an electric field is swept back and forth along the direction of the cut, the polarization shows the two stage reversal behaviour shown in Fig.2.8 (b) provided that the maximum amplitude of the field is bigger than a critical value.

Initially, the strong positive field fully poles the material along  $[011]$ . This results from a multi-domain configuration where the local polarization vectors align to either the  $[111]$  or the  $[\bar{1}\bar{1}\bar{1}]$  variants. Upon reversal of the applied field, the polarizations switch to the  $[\bar{1}\bar{1}\bar{1}]$  and  $[111]$  directions respectively. Such switching is mediated by a narrow range around the coercive field,  $E_c$ , in which the polarizations point along the in-plane  $[100]$  and  $[011]$  variants. The latter is accompanied by tensile and compressive strains in the two orthogonal axes according to the piezoelectric coefficients  $d_{31} = 610\text{pC/N}$  and  $d_{32} = -1883\text{pC/N}$ . As a result, a large strain anisotropy of the order of  $10^{-3}$  is generated in the plane near  $E_c$ , Fig.2.8 (c).

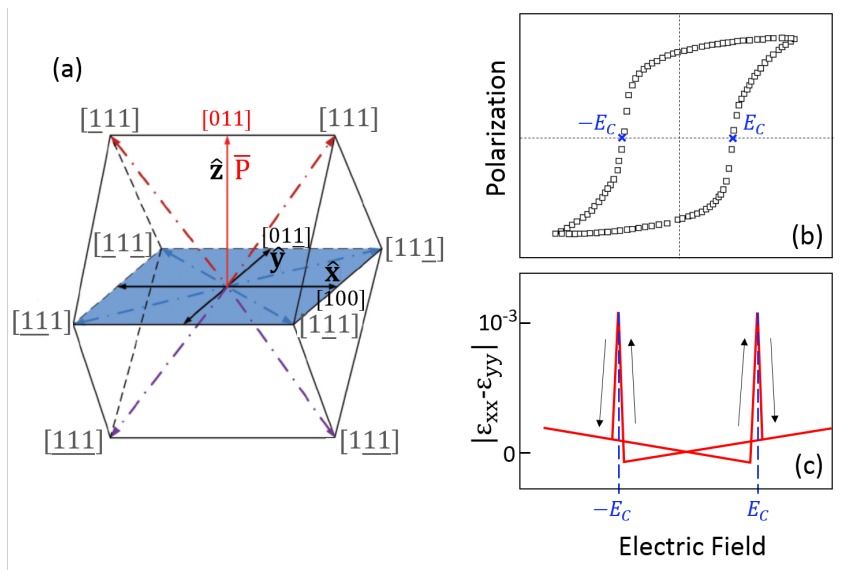


Figure 2.8: (a) Rhombohedral phase of PMN-PT with  $[011]$  orientation, adapted from [29]; (b) polarization [30] and (c) strain anisotropy [31] as a function of the amplitude of the electric field applied along the direction of the thickness,  $[011]$ .

It has also been reported that a localized strain anisotropy can be produced between a pair of electrodes patterned on top of a ferroelectric substrate [32]. The structure, which consisted of a PZT substrate with two 100nm aluminium (Al) square electrodes on top, is shown in Fig.2.9.

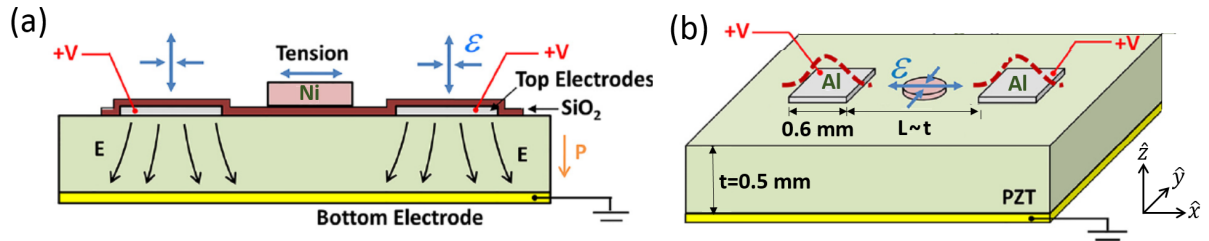


Figure 2.9: Schematic of the device that generates localized bi-axial surface strain that interacts with the magnetostrictive element. (a) Cross section and (b) isometric view. The dashed line in (b) illustrates the out-of plane expansion under the electrodes that creates the bi-axial strain field  $\epsilon_{xx} - \epsilon_{yy} > 0$  in a central Ni island [32].

With the back fully grounded, a voltage  $V$  is applied to the upper electrodes. As a result, the piezoelectric material underneath expands and contracts along  $\hat{x}$  and  $\hat{y}$  respectively. In order to accommodate the in-plane deformation, mechanical stretching of the PZT occurs in the space between the two electrodes as well. Consequently, the magnetic Ni element located between the latter is elongated along  $\hat{x}$  ( $\epsilon_{xx} > 0$ ) and contracted along  $\hat{y}$  ( $\epsilon_{yy} < 0$ ), leading to a bi-axial strain anisotropy  $\epsilon_{xx} - \epsilon_{yy} > 0$  within the device.

Magnetic domain wall motion [19] and chirality switching of a vortex domain wall [31] has already been observed in Ni ring/(011)PMN-PT heterostructures where the strain anisotropy of  $\approx 10^{-3}$  induces a magnetoelastic anisotropy (2.21) of the order of  $10\text{kJ/m}^3$  ( $B_1 \approx -6.2\text{MJ/m}^3$ ). Regarding flux-closure vortex states, distortion of the in-plane magnetic domains has been observed for  $\text{Fe}_{81}\text{Ga}_{19}$  discs<sup>4</sup> with a diameter of  $\approx 2\mu\text{m}$  coupled to a PZT transducer. When a voltage is applied to the transducer, a uniform tensile strain of  $\approx 10^{-4}$  is generated, which induces a uniaxial anisotropy of  $\text{kJ/m}^3$  along [010] ( $B_1 \approx 16\text{MJ/m}^3$ ). The strain-induced uniaxial anisotropy aligns the magnetization more strongly along the anisotropy axis, enlarging the domains whose magnetization points along [100] and shrinking the domains whose magnetization aligns along [010]. However, due to the symmetry of the system, the vortex core is not displaced from the centre of the element, as can be seen in Fig.2.10.

<sup>4</sup>The disc structure in this case forms a Landau flux-closure similar to the normally found in square elements, rather than the usual curling vortex structure. This is due to the strong magnetocrystalline cubic anisotropy of  $\text{Fe}_{81}\text{Ga}_{19}$ .

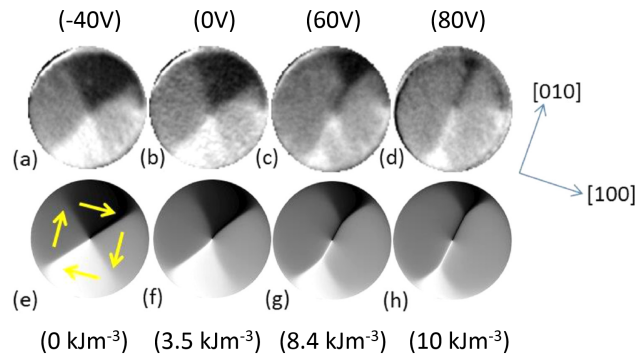


Figure 2.10: On top, evolution of the magnetic domain pattern in a  $2.2\mu\text{m}$  circular  $\text{Fe}_{81}\text{Ga}_{19}/\text{PZT}$  structure for different voltages applied to the transducer. On the bottom, micromagnetic simulations of the  $\text{Fe}_{81}\text{Ga}_{19}$  device with an uniaxial anisotropy along  $[010]$  given by  $K_s$  equal to (e) 0, (f) 3.5, (g) 8.4, and (h)  $10\text{kJ}/\text{m}^3$ . The yellow arrows indicate the direction of the magnetization in each domain [18].

In [16] Ostler et al. show that this symmetry can be broken by introducing a 1-dimensional linear gradient in the magnitude of the strain-induced anisotropy of the form  $\epsilon(y) = (d\epsilon/dy)y$ . The present work extends this idea and investigates the effect of the strain induced anisotropy gradient on the vortex core displacement for Ni/PE and  $\text{Fe}_{81}\text{Ga}_{19}/\text{PE}$  heterostructures and discusses the experimental implementation of the gradient by means of a PMN-xPT ( $x \approx 0.32$ ) substrate. Both square and circular vortex geometries are considered.

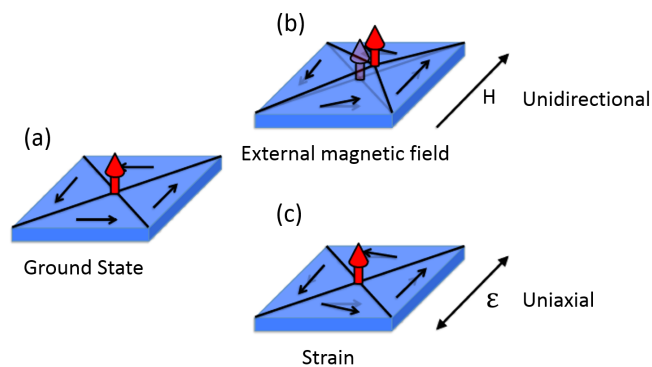


Figure 2.11: Sketch of a square device in a flux closure vortex state (a), showing how a unidirectional anisotropy introduced by a magnetic field can displace the vortex core (b), in contrast to the uniaxial anisotropy induced by the strain (c) which cannot shift the core, adapted from [16].

# Chapter 3

## Method

### 3.1 Micromagnetic simulations

The initial part of this project was to simulate the effects of a strain gradient in  $\text{Fe}_{81}\text{Ga}_{19}$  and Ni micron-sized devices with the micromagnetic solver OOMMF (Object Oriented Micromagnetic Framework).

OOMMF is a numerical finite difference solver for solving problems defined on a 3D grid of square cells holding 3D spins. The code works by solving the LLG equation (2.27), as well as finding the ground state of a magnetic body by minimizing equation (2.23). In this work, the minimization method was used in order to find the ground state of the system when a strain induced anisotropy gradient was introduced.

With OOMMF, the ferromagnetic body is divided into cuboids of dimensions  $\Delta_x, \Delta_y, \Delta_z$  called cells and a uniform magnetization inside each cell  $\vec{m}_i$  is assumed. Then, given a certain initial state, the energy of the system is computed cell by cell. In this discrete model, the expressions for the exchange, the cubic and uniaxial anisotropies and the Zeeman energy densities at cell  $i$  are defined by<sup>1</sup>:

$$U_{exch_i} = \sum_{j \in N_i} A_{ij} \frac{\vec{m}_i \cdot (\vec{m}_i - \vec{m}_j)}{\Delta_{ij}^2} \quad (3.1)$$

$$U_{can_i} = -K_u \left( \alpha_1^{i2} \alpha_2^{i2} + \alpha_2^{i2} \alpha_3^{i2} + \alpha_3^{i2} \alpha_1^{i2} \right) \quad \text{where} \quad \alpha_k^i \ (k = 1, 2, 3) = \vec{m}_i \cdot \vec{u}_k. \quad (3.2)$$

---

<sup>1</sup>Note that OOMMF adds a minus sign to the cubic anisotropy energy (3.2) and the uniaxial anisotropy energy (3.3) redefining the anisotropy constants  $K_c$  and  $K_u$  respectively.

$$U_{uan_i} = -K_u(\vec{m}_i \cdot \vec{u})^2 \quad (3.3)$$

$$U_{z_i} = -\mu_0 M_s (\vec{m}_i \cdot \vec{H}_{ext}) \quad (3.4)$$

Specifically, 3.1 is the expression for the exchange energy of the  $i^{th}$  cell coupled to its nearest 6 neighbouring cells, which is obtained by substituting the derivatives in 2.5 with finite differences.  $N_i$  is the set of the 6 cells nearest to the  $i^{th}$  cell and they are coupled to the latter via the corresponding stiffness coefficients  $A_{ij}$ . Finally,  $\Delta_{i,j}$  is the discretization step size between two cells  $i$  and  $j$ , and it is defined as the distance in meters between the central points of the two cells. The only term missing is the magnetostatic term. This is the hardest one to compute and involves Fourier Transforms in the process. First, the demagnetizing field at each cell is computed:

$$\vec{H}_{d_i} = \sum_j \overline{\overline{N}}_{i,j} \vec{m}_j \quad (3.5)$$

where  $\overline{\overline{N}}_{i,j}$  is the demagnetizing tensor defining the demagnetizing field arising from cell  $j$  at cell  $i$ , which is computed using the formulae in [33]. The total demagnetization energy is then determined by the convolution of the individual cells with Fast Fourier Transforms. Once the energy of the initial state has been calculated, the state of minimum energy is searched iteratively through the method of conjugate gradients.

In this study,  $2\ \mu\text{m} \times 2\ \mu\text{m}$  Galfenol and nickel squares have been simulated, as well as some  $2\ \mu\text{m}$ -diameter Ni discs. In all the cases, the thickness of the devices was 20 nm. The cubic anisotropy typical of these materials was neglected because its contribution to the energy is much smaller than the uniaxial anisotropy term that will be introduced ( $K_c \ll K_u$ ), as polycrystalline sputtered samples are assumed. All in all, the material parameters used as inputs are specified in table 3.1. All the calculations have been done using a rectangular mesh of  $5\text{nm} \times 5\text{nm} \times 10\text{nm}$  cells.

	<b>Fe<sub>81</sub>Ga<sub>19</sub></b>	<b>Ni</b>
<b>Ms (A/m)</b>	$1.378 \times 10^6$	$2.1 \times 10^5$
<b>A (J/m)</b>	$1.3 \times 10^{-11}$	$10^{-11}$
<b>Kc (J/m<sup>3</sup>)</b>	0	0

Table 3.1: Material parameters used in our OOMMF simulations for Galfenol and nickel.

The initial state for all the simulations has been a Landau structure with a vortex core at the centre defined by an anti-clockwise chirality and positive polarity. Such a state had been previously simulated starting from the Landau configuration in Fig. 3.1, introduced as a bitmap image, and applying a magnetic field along  $+\hat{z}$  through the Zeeman term. (3.4).

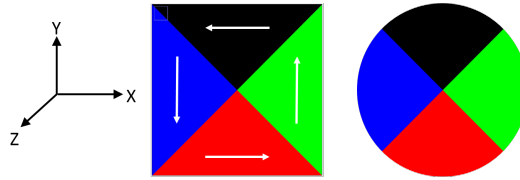


Figure 3.1: Bitmap images for the square and circular geometries used to calculate the initial vortex state with OOMMF. White arrows represent the direction of the magnetization depending on the colour of the domain.

## 3.2 Design of the samples

In order to implement the in-plane strain anisotropy gradient  $\Delta\epsilon(y)$ , three experiments were designed. The strain is generated in a PMN-PT substrate by applying a voltage to Au contacts and making use of the high piezoelectric coefficients of the PMN-PT. The 3 experiments, E1, E2 and E3, were carried out using two different samples which have been represented schematically in Fig.3.2 (a) and Fig.3.2 (b).

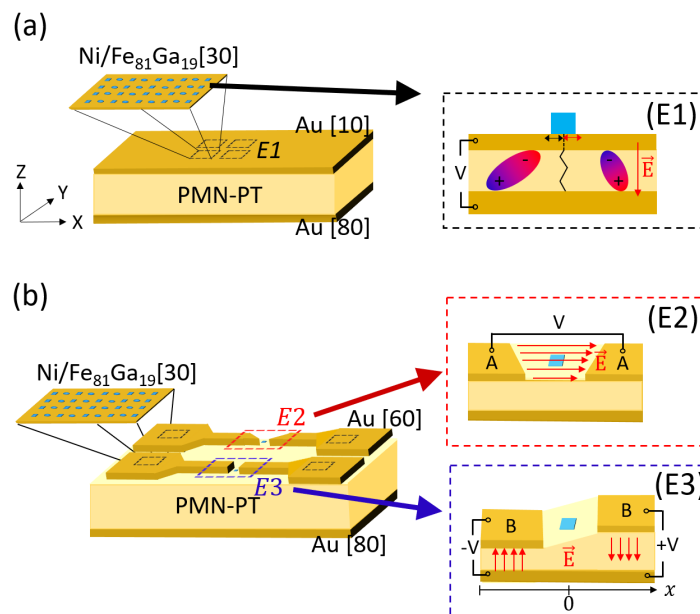


Figure 3.2: Sketch of the two FM/PE structures that were fabricated for the generation of an anisotropy gradient in the magnetostrictive elements represented in blue. The thicknesses in brackets are expressed in nm. Within the dashed frames, it is illustrated how a strain gradient is achieved for each experiment E1, E2 and E3.

In E1, Fig.3.2 (E1), the upper electrode is a uniform layer of gold (Au) that covers the entire polished surface of the PMN-PT plate. On top of the latter, the ferromagnetic devices (in blue) are located at the areas delimited by the black dashed lines. Devices include square and circular elements of several dimensions that range from 0.5  $\mu\text{m}$ - to 6  $\mu\text{m}$ -diameter and side respectively. In this design a strain gradient can be accomplished due to the ferroelectric domain states of the PMN-PT. It is known that ferroelectric domains in PMN-PT can range from tens [34] or hundreds [35] of nm up to several tens of  $\mu\text{m}$  [36], and such domains can represent different polarization and structural phases [37].

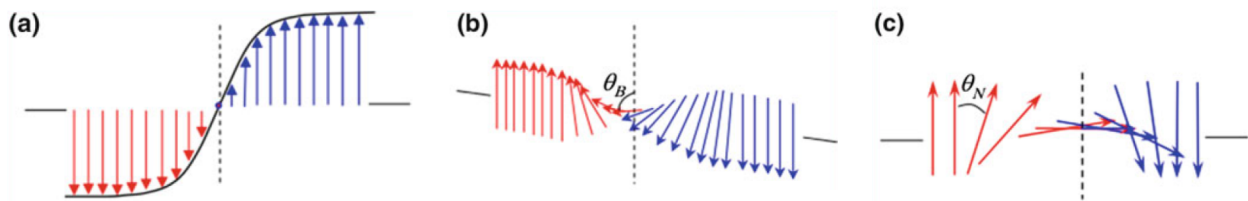


Figure 3.3: Different types of domain walls. (a) Ising type, showing a gradual magnitude variation but no spin rotation. (b) Bloch type, showing a gradual rotation parallel to the domain wall. (c) Néel type, showing a normal rotation to the domain wall. From (a) to (c) the width of the domain wall increases. Taken from [38].

Unlike ferromagnetic materials where Bloch and Néel walls are present (§ 2.1.3), ferroelectric domain walls are predominantly Ising type. Indeed, the coupling between ferroelectric polarization and lattice strain imposes a significant energy cost for rotating the polarization away from the symmetry-allowed directions in the lattice, which leads to much narrower domain walls with only several nanometres width (see Fig.3.3). Hence, it is quite likely that one of the elements sits somewhere on top of a multi-ferroelectric domain area. Localized strain gradients can arise within such a small area containing domain boundaries where several phases join, each phase leading to strain of a different nature.

In the second experiment, E2, patterned top electrodes were used to create a localized strain gradient between a pair of top electrodes A-A where a 2  $\mu\text{m}$  square is located. The electrodes consist of 1.0 mm  $\times$  1.5 mm square pads separated by a distance of approximately 2mm to allow an easy contact between these and the back electrode. In order to generate a gradient in the region around the 2 micron island, a 0.5 mm-long arm rises from each pad and faces the ferromagnetic element. As can be observed in

Fig.3.2 (E2), the arms are wedge shaped towards the ferromagnetic device and thus the island-electrode distance varies linearly on  $\hat{y}$  from  $\approx 5 \mu\text{m}$  to  $\approx 6.25 \mu\text{m}$ . This way, when a voltage is applied between the electrodes, the resulting electric field also varies in  $\hat{y}$ . Such an electric field can penetrate the piezoelectric and propagate through the surface, producing an  $\hat{y}$ -dependent in-plane strain  $\Delta\epsilon(y)$  according to<sup>2</sup>  $d_{12} = -1340\text{pC/N}$ .

In E3, another pair of electrodes B-B faces a similar 2 micron square. However, the arms emerging from the pads are no longer wedge shaped at their end. The gradient here arises when a negative voltage is applied to one of the B electrodes and a positive voltage to the other electrode while the bottom is grounded. As a consequence, the PMN-PT suffers a mechanical deformation in  $\hat{z}$  that goes from a contraction at one end of the substrate (at  $-\hat{x}$ ) to an expansion at the other end (at  $+\hat{x}$ ). The out of plane contraction is followed by an expansion in  $\hat{y}$  ( $d_{32} = -1883\text{pC/N}$ ), whereas the expansion in  $\hat{z}$  leads to a contraction along the latter. The opposite occurs for the  $\hat{x}$  direction ( $d_{31} = +610\text{pC/N}$ ). This results in an in-plane strain gradient along  $\hat{x}$ ,  $\Delta\epsilon(x)$ , as shown in Fig.3.2 (E3).

### 3.3 Experimental techniques

#### 3.3.1 Fabrication techniques

The two samples in § 3.2 were fabricated using one surface polished PMN-PT ( $x \approx 0.32$ ) single crystal plates acquired from Atom Optics Co., cut into  $5\text{mm} \times 5\text{mm} \times 0.3\text{mm}$  substrates. The Au electrodes were thermally evaporated, using e-beam lithography for the patterned contacts. The ferromagnetic devices were also fabricated using e-beam lithography. In this case, the deposition of the ferromagnetic Ni and  $\text{Fe}_{81}\text{Ga}_{19}$  30-nm layers was carried out by collaborators at The University of Nottingham via magnetron sputtering. A capping layer of chromium was also deposited to avoid oxidation. Below, thermal evaporation and e-beam lithography will be described in more detail.

##### 3.3.1.1 Thermal evaporation

Thermal evaporation is a thin-film deposition method where the source material is evaporated in a vacuum and deposited on the substrate. The vacuum allows vapour particles to travel directly to the target, where they condense back to a solid state. Using

<sup>2</sup>The values for the piezoelectric coefficients of the PMN-PT have been obtained from [39].

the MANTIS HEX deposition system shown in Fig.3.4 (a), a thick 80-nm layer of gold was put down on the polished side of the PMN-PT as the back contact. On the other side, the thinner top electrodes were deposited.

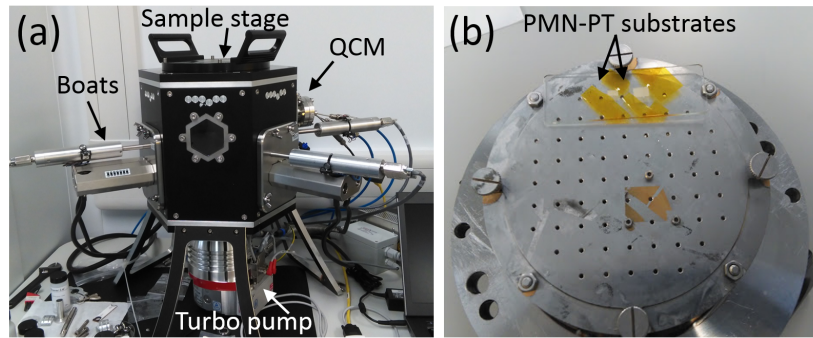


Figure 3.4: (a) Mantis system of thermal evaporation and (b) PMN-PT substrates fixed to the sample holder prior to deposition.

The PMN-PT is mounted into the sample holder as shown in Fig.3.4 (b). Subsequently, this is loaded in the vacuum chamber with the substrate facing downwards. After loading the substrate, the main chamber was pumped down to at least  $5 \times 10^{-6}$  mbar.

The MANTIS system is fitted with three thermal boat sources on the bottom of the chamber, one of which was loaded with gold in the form of little solid pellets. Boats are essentially thin sheet pieces of suitable metals which can be heated to very high temperatures with electric currents. The gold inside the boat is heated to its melting point producing some vapour pressure inside the chamber. In high vacuum conditions, a vapour cloud is produced, which traverses the chamber, impinges on the PMN-PT substrate and sticks to it as a thin film. During this process, the thickness of the deposited Au film is measured by the Quartz Crystal Microbalance (QCM) located close to the substrate, which resonates at different frequencies depending on the additional mass deposited during the evaporation.

The same procedure was carried out to deposit the upper Au layer onto the non-polished side of the PMN-PT. All the depositions were carried out with a current between 55 A and 70 A, with which a deposition rate between 0.3 and 0.6 Å/s was achieved. After the desired thickness was reached, the shutters of the boat were closed and the current was ramped down to 0 A to end the depositions.

### 3.3.1.2 Electron Beam Lithography (EBL)

The Raith VOYAGER e-beam lithography system enabled the fabrication of the pairs of patterned top electrodes in experiments E2 and E3, as well as all the square- and disc-shaped ferromagnetic elements.

Through this technique, the desired pattern is written out as a nanometre sized focussed electron beam is moved over the sample. Such a pattern is recorded in an electron sensitive film (e-resist) that is deposited before the exposure by spin-coating. The e-beam induces a change in the molecular structure of the resist and as a result, either the exposed or the unexposed areas of the latter can be dissolved in a solvent called developer. The pattern can then be transferred to the material deposited on top through a lift-off procedure. All these steps involved in the lithography process are illustrated in Fig.3.5.

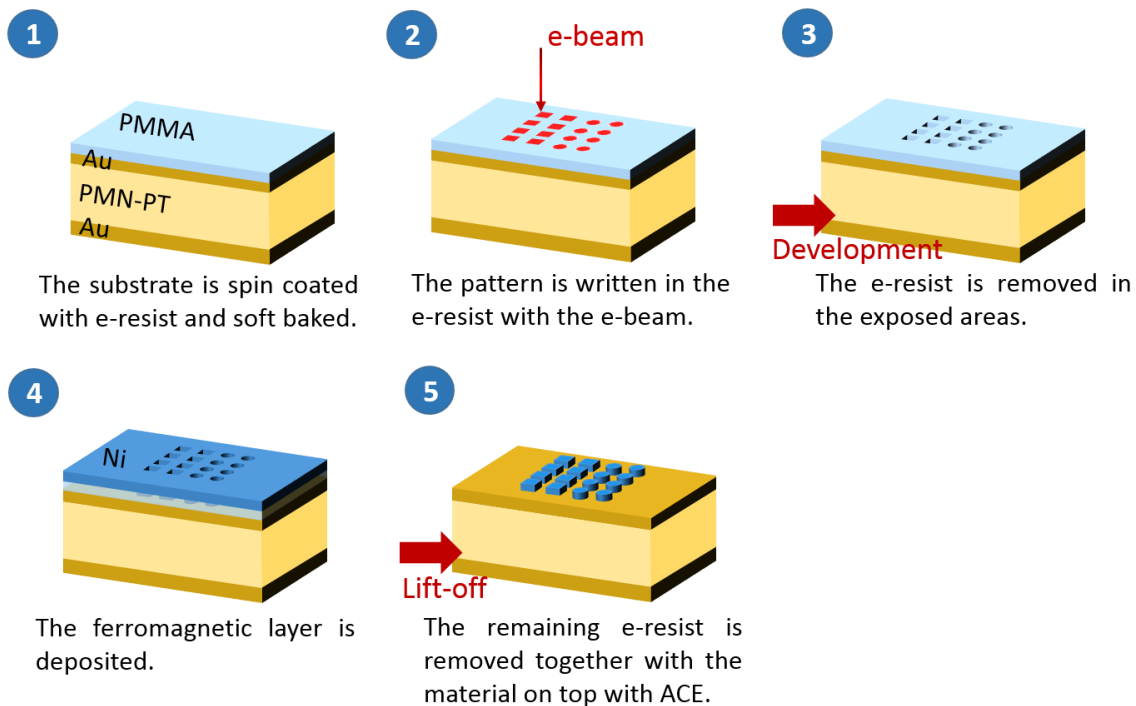


Figure 3.5: Schematic representation of the e-beam lithography process for the ferromagnetic devices in E1.

A 950 PMMA (poly-methyl methacrylate) resist was used for all the samples, deposited on the substrate using spin coating at 4000 rpm for 60 seconds and subsequently soft-baked. Because the PMN-PT is a pyroelectric material, the baking was carried out by using slow ramps and reaching no higher temperatures than 150C°. The PMMA is a positive tone resist, which means that it is the exposed areas that are dissolved during

the development. The developer was a solution mixture of isopropanol (IPA) and de-ionized (DI) water in a ratio of 7:3.

The pattern is transferred to the material (Au in the case of the electrodes and Ni or Fe<sub>81</sub>Ga<sub>19</sub> in the case of the devices) by dissolving the remaining resist in acetone (ACE), which lifts off the material on top so that only the material that was deposited in the areas where there was no resist is left.

To write the pattern with the e-beam, Fig.3.5 step 2, a write field of 500 μm and a step-size of 5 nm were used. That is, for a fixed stage position, a maximum area of 500 μm was written, during which the beam moved in steps of 5 nm until it had gone through the entire area. One of the most relevant quantities that determines the quality of the pattern is the dose, which must be sufficient to fully remove all the exposed regions but not so big that the non-exposed areas are removed as well. The dose of exposure depends on the step size, as well as on the beam current and the dwell time (time that the beam stays still in a given position):

$$\text{Area dose} = \frac{\text{Beam current} \cdot \text{Dwell time}}{\text{Step size}^2} \quad (3.6)$$

For the square contacts a dose of 3300 μC/cm<sup>2</sup> was used with a beam current of 5859.6 pA and an aperture of 100 μm. For the devices, which require higher sensitivity, a smaller beam current of 651.61 pA was set with an aperture of 40 μm. In this case, a dose range between 230 μC/cm<sup>2</sup> to 825 μC/cm<sup>2</sup> was covered for each element in order to ensure the right dose for each size and shape in the pattern.

### 3.3.1.3 Demagnetization routine

Whereas micron-sized Galfenol and Permalloy discs and squares are usually found in a flux-closure vortex state right after their fabrication, this is seldom the case for Ni devices. Nickel has a lower saturation magnetization, and therefore the shape anisotropy (2.17), which is responsible for the flux closure state, is weaker in this material. As a consequence, unavoidable defects at dislocations and non-magnetic inclusions cause pinning sites that prevent the Ni elements to be in their otherwise natural ground state. One way to bring the Ni elements to the desired flux-closure vortex configuration, is to apply a low frequency magnetic field whose amplitude decreases linearly as shown in

Fig.3.6 (a).

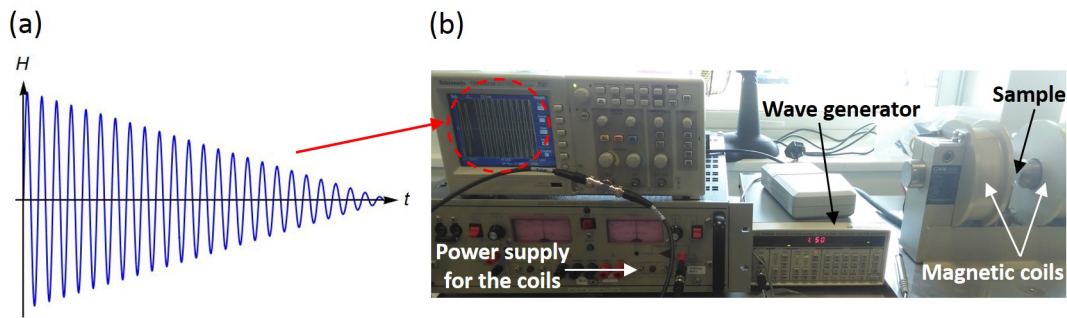


Figure 3.6: (a) Depiction of the amplitude modulated magnetic field used in the demagnetization routine. (b) Experimental set up used to bring the Ni devices to a flux closure vortex state.

When the amplitude of the oscillating field is maximum, the magnetic moments in the devices will follow its direction. As the amplitude of the field decreases, the magnetization will lose gradually the track of the field, until at 0 amplitude it will no longer be influenced by the latter. At that point, the magnetic field is switched off. This way, whatever the magnetic domain walls were formed upon fabrication, they can be unpinned and a new ground state is reached. In order to create a magnetic field of this form, the set up in Fig.3.6 (b) was utilized. A couple of magnetic coils were fed with a sine wave of  $1.5V_{pp}$  and 0.5Hz which was amplitude modulated by a triangular wave of 0.005Hz. This led to a 0.5Hz magnetic field inside the coils with a maximum amplitude of  $\approx 45mT$  sufficient to initially saturate the nickel devices.

### 3.3.2 Imaging techniques

In order to look at the magnetic configuration of the devices and track the position of the vortex core, XMCD and MFM measurements were performed, which will be described in this section.

#### 3.3.2.1 X-Ray Magnetic Circular Dichroism (XMCD)

X-ray magnetic circular dichroism or XMCD is the phenomenon that refers to the difference in absorption of right handed ( $\sigma^+$ ) and left handed ( $\sigma^-$ ) circular polarized x-rays at an inner-shell absorption edge of a magnetic material.

In a transition metal such as nickel ( $3d^9$ ), magnetic properties can be extracted from  $2p \rightarrow 3d$  electronic transitions. The  $2p$  level is split into  $2p_{1/2}$  and  $2p_{3/2}$ , which

correspond to an anti-parallel ( $j = l - s$ ) and a parallel ( $j = l + s$ ) spin-orbit coupling respectively. This results in the  $L_2$  ( $2p_{1/2} \rightarrow 3d$ ) and  $L_3$  ( $2p_{3/2} \rightarrow 3d$ ) edges in the x-ray absorption spectrum with intensities  $I_2$  and  $I_3$ .

When circularly polarized x-rays impinge on the sample, photons transfer their orbital angular momentum to the core electrons in the  $2p_{1/2}$  and  $2p_{3/2}$  levels. Due to the spin-orbit coupling, for a given circular polarization, a different number of spin-up and spin-down photoelectrons are generated from any of the 2p levels. For a right circular polarized light 62.5% (37.5%) spin-up (spin-down) photoelectrons are generated from  $2p_{3/2}$ , whereas 25% (75%) are generated from  $2p_{1/2}$ . For  $\sigma^-$  the percentages are reversed as the photons carry an opposite angular momentum. Here, spin-up and spin-down are defined relative to the photon helicity.

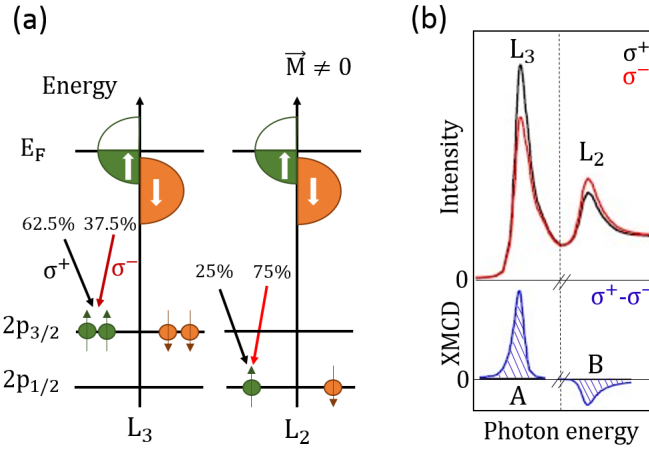


Figure 3.7: (a) Schematic depiction of the two-step mechanism of the XMCD. In this case, there are only unfilled spin up states which makes the detector only sensitive to spin up states. As a result,  $I_3$  is then higher for  $\sigma^+$  than for  $\sigma^-$  and the opposite happens regarding  $I_2$  (b). Subtracting the two intensities  $I(\sigma^+) - I(\sigma^-)$ , the so-called XMCD signal is positive at  $L_3$  (peak A) and negative at  $L_2$  (peak B).

When the sample is magnetic, the exchange-split  $3d$  valence band acts as a spin-sensitive detector. Due to the imbalance between spin-up and spin-down d-holes, the transition of either spin up or spin down electrons is favoured. The quantization axis of this detector is given by the direction of the magnetization. The resulting dichroism effect, that is, the subtraction of the absorption peaks acquired for the two different polarizations of the x-rays, is proportional to the difference between the spin-down and spin-up holes which is in turn, proportional to the magnetic moment per atom:

$$I_{2,3}^{XMCD} = I_{2,3}(\sigma^+) - I_{2,3}(\sigma^-) \propto \vec{\mu} \cdot \vec{\sigma} \quad (3.7)$$

where  $\vec{\sigma}$  is the handedness of the photons. As can be seen, the dichroism is maximum when the magnetization of the sample lies along the direction of the incident light. In that case, the magnetization pointing parallel and anti-parallel to the x-rays leads to a sign difference in the XMCD signal and an image contrast is obtained.

### 3.3.2.2 X-Ray Photoemission Electron Microscopy (X-PEEM)

When photoelectrons are excited, the resulting core holes often decay via an Auger process. That is, when the vacancy left by the photoelectron is filled by an electron from a higher energy level, the resulting release of energy can be transferred to another electron which is ejected from the atom. The ejected electrons are known as secondary electrons. A PEEM microscope measures the x-ray absorption indirectly by imaging the secondary electrons yield from the sample. If installed in a synchrotron beam line where x-rays of the adequate wavelengths are produced, the so-called X-PEEM can be used to perform magnetic imaging with XMCD as the contrast mechanism (Fig.3.8), measuring the projection of the magnetization along the direction of the photon.

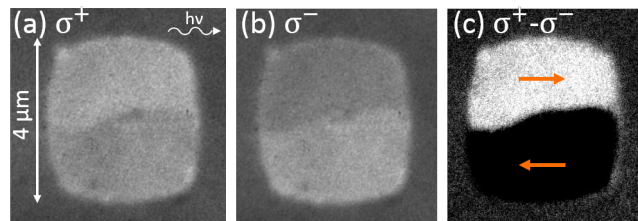


Figure 3.8: X-PEEM images of a Ni square obtained at the Ni  $L_3$  edge using circularly polarized photons with (a) positive helicity ( $\sigma^+$ ) and (b) negative helicity ( $\sigma^-$ ). (c) The difference signal ( $I^+ - I^-$ ), XMCD, clearly shows 2 magnetic domains in the element. The direction of the magnetization in each domain is represented by the orange arrows.

At Diamond Light Source (DLS), beam line I06 combines PEEM with polarised soft X-rays, enabling XMCD measurements. What is more, the system in I06 allows electric fields to be applied to the sample in situ. In this work, this beamline was used to measure Ni/PMN-PT devices under external voltages between  $-200\text{V}$  and  $200\text{V}$ . The Ni elements were measured by tuning circularly polarized x-rays to the  $L_3$  edge at  $852.7\text{ eV}$ . For each measurement, 10 images were taken for a positive polarization first, and other 10 were taken for a negative polarization afterwards. The procedure was then repeated for a lower energy, at the so-called pre-edge (pe). The polarization and the energy of the beam can be changed through two couples of PPM (pure permanent magnets) arrays called undulators, which can be arranged in different ways to produce different magnetic fields.

After properly averaging and normalizing the images taken at each polarization (3.8), the resulting images are subtracted to obtain an asymmetric image with magnetic contrast  $I_{XMCD}$ .

$$I_{XMCD} = \frac{\sum_{i=1}^{10} I_3^i(\sigma^+)}{\sum_{i=1}^{10} I_{pe}^i(\sigma^+)} - \frac{\sum_{i=1}^{10} I_3^i(\sigma^-)}{\sum_{i=1}^{10} I_{pe}^i(\sigma^-)} \quad (3.8)$$

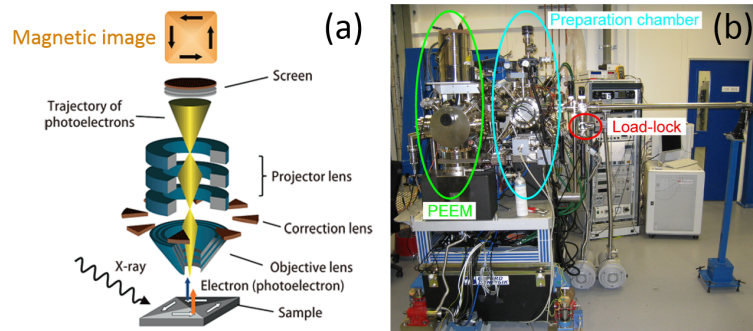


Figure 3.9: (a) Sketch of a PEEM microscope used to image magnetic domains by bombarding the sample with circularly polarized x-rays, taken from [34]. (b) PEEM in the I06 beamline at DLS.

### 3.3.2.3 Magnetic force microscopy (MFM)

Magnetic force microscopy (MFM) is another magnetic imaging technique that can also be used to image vortex structures [21]. This is an in-house technique easier to perform compared to X-PEEM measurements which require beam-time at an external facility such as DLS. At the York JEOL Nanocentre, MFM measurements can be done using the BioScope Resolve system shown in Fig.3.10.

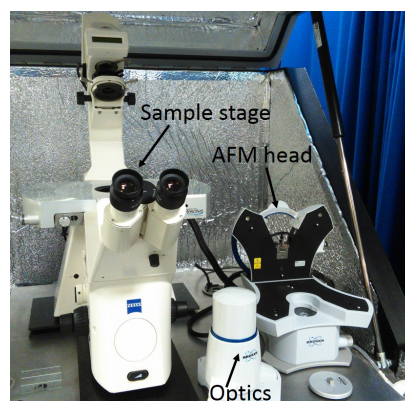


Figure 3.10: BioScope Resolve system from Bruker at the York JEOL Nanocentre.

MFM is an imaging technique based on atomic force microscopy (AFM). In MFM a magnetic-coated tip attached to a flexible cantilever moves over the sample surface along

parallel lines divided into many pixels. Through a dithering piezo, the cantilever is vibrated at or slightly off its resonance frequency. During the raster scan, the interactions between the tip and the surface produce changes in the frequency, amplitude and phase of the oscillations of the cantilever. These changes can then be monitored through a laser beam focussed on the back of the cantilever, which is reflected and detected by a position sensitive photodiode.

In a first scan, the tip is driven very close to the sample surface (at 15-25 nm) where short-range atomic and van der Waals forces dominate. Phase and amplitude changes produced by these forces are detected by the photodiode and converted into electric signals  $V(t)$ . The difference between the amplitude and a reference value  $V_0$  is then minimized through a feedback loop whose output is the signal that has to be applied to the Z-piezo scanner to keep the oscillation amplitude constant. This way, the topography of the sample is mapped. The process is schematically represented in Fig.3.11 (a).

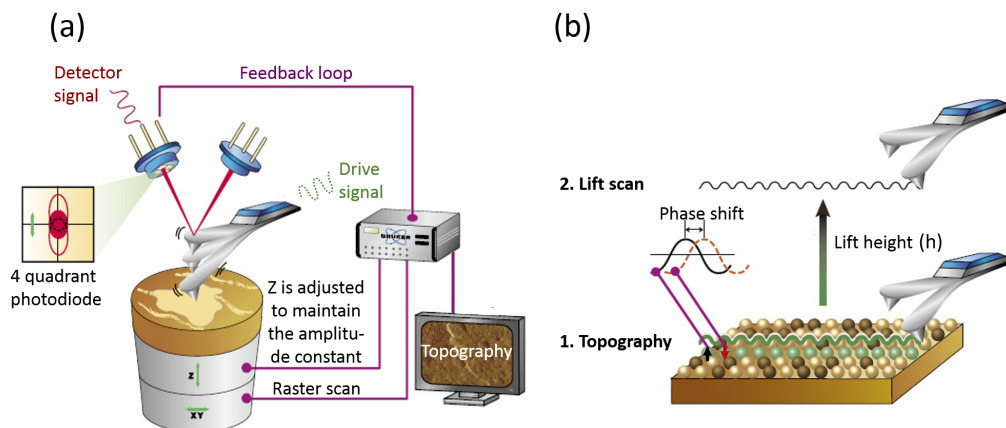


Figure 3.11: (a) Depiction of the atomic force microscopy where a tip attached to the cantilever scans the sample surface to gather topographic information. (b) Sketch of the magnetic force microscopy where the tip is lifted and the magnetic interaction between tip and sample is measured. Adapted from [40].

In MFM the tip is raised to a height  $h$  and a second scan is performed where the tip-surface distance is kept constant by following the topographic profile as Fig.3.11 (b) shows. This way, contributions from the previous forces are minimized allowing relatively weak but long-range magnetic interactions to be detected. The magnetostatic interaction between the magnetic tip and the stray fields arising from the sample is given by:

$$\vec{F} = \mu_0 \int_V \vec{\nabla} \cdot (\vec{M}_{tip} \cdot \vec{H}_{sample}) dV_{tip} \quad (3.9)$$

where  $\vec{M}_{tip}$  is the magnetic configuration of the tip. The tip has a sharp cone-like shape whose magnetization points along the perpendicular to the sample. As a consequence, (3.9) is reduced to the interaction with the out of plane component of the stray fields,  $H_{sample,z}$ :

$$F = F_z = \mu_0 \int_V \frac{\partial}{\partial z} (M_{tip,z} \cdot H_{sample,z}) dV_{tip} \quad (3.10)$$

The force gradient along the vertical  $\frac{\partial F_z}{\partial z}$  alters the resonant characteristics of the cantilever by shifting the oscillation frequency. Such a shift is measured as a change in the amplitude  $\delta A$  or a change in the phase  $\delta\phi$  with respect to the driving signal. If the cantilever is excited at the free resonance, the sign of  $\delta A$  is insensitive to the sign of the force gradient. However, the phase shift is:

$$\delta\phi = -\frac{Q}{k} \frac{\partial F_z}{\partial z} \quad (3.11)$$

Here,  $Q$  is the quality factor of the cantilever and  $k$  is the spring constant that models the deflection of the cantilever. Attractive interactions  $\frac{\partial F_z}{\partial z} > 0$  give negative phase shifts whereas repulsive interactions  $\frac{\partial F_z}{\partial z} < 0$  lead to positive phase shifts. This forms an image contrast between domains pointing parallel,  $+\hat{z}$ , or anti-parallel,  $-\hat{z}$ , to the surface normal. For an in-plane magnetized sample, domain walls lifting out-of plane can also be observed.

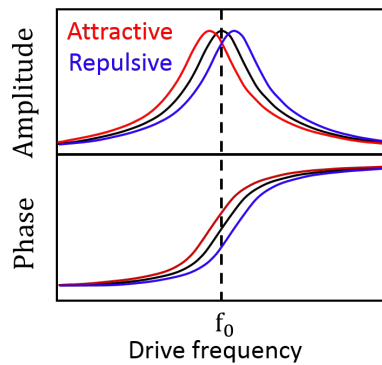


Figure 3.12: Frequency shift arising from the magnetic interaction between the tip and the sample, which is measured either by a change in the amplitude or a change in the phase respect to the driving signal.

The 30–60 nm lateral resolution of the BioScope Resolve system may not resolve a vortex core (with a expected diameter of  $\approx 20$  nm) in the ferromagnetic elements. However, the domain walls of the in-plane Landau structure can be imaged in the square-shaped elements, which is sufficient to track the position of the core.

Nevertheless, magnetic imaging with the BioScope Resolve at York was a big challenge. Several issues had to be overcome before achieving the first magnetic image, including software and hardware problems that left the system unavailable for more than one month. A couple of test samples of known magnetic state were used first, including the following waveguide with Permalloy structures on it:

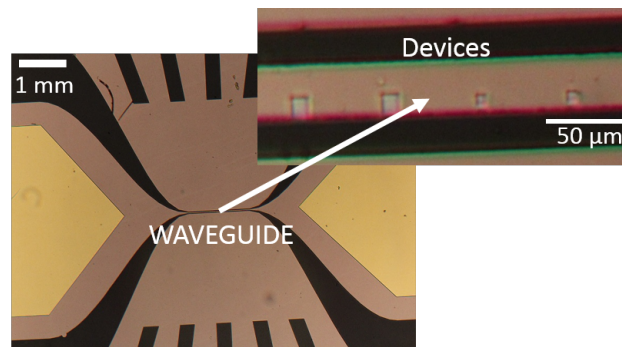


Figure 3.13: Micrograph of the waveguide used as a test sample to image with the MFM. Inside the waveguide there are lots of different devices of Permalloy that were imaged with the MFM.

Devices in the waveguide include discs, ellipses, rectangles and squares with sizes from hundreds of nanometres to several microns, some of them in a flux-closure state.

The main reason why magnetic imaging was so difficult was the lack of suitable probes to do the measurement. PPP-LM-MFMR probes from Nanosensors were used in the beginning, which were the only probes with magnetic coating available at the Nanocentre. One of the measurements performed with these probes can be observed in Fig.3.14 (a), where the phase channel of the lift scan is shown for one of the devices in the waveguide. Even if a strong magnet was used to try to restore the magnetization of the tip, magnetic contrast was never observed but only topographical information. After many unsuccessful measurements, this seemed to indicate that the probes were too old and had lost magnetic sensitivity over time.

New probes were then ordered from Bruker, MESP-LM-V2 probes, cobalt-chromium coated. Using a strong magnet again to magnetize the tip perpendicular to the probe, a Flux Closure pattern could finally be imaged in the same device, a  $2\ \mu\text{m} \times 2\ \mu\text{m}$  square, shown in Fig.3.14 (c). Magnetic contrast was observed in a range between 25 nm and 50

nm height providing that the laser had been properly aligned on the cantilever and the photodetector had been properly adjusted. Otherwise, as magnetic forces are weak, the magnetic contrast could be lost relatively easily, Fig.3.14 (b). The optimum lift height to image the Permalloy square was found to be between 30 and 40 nm. In the image, 4 in-plane magnetic domains are distinguished separated by the domain walls which interact with the magnetic tip. The cross formed by the walls matches the  $M_z$  profile of the simulated Landau vortex state, Fig.4.1 (a) in § 4.1.1, except that the core is too small to be resolved.

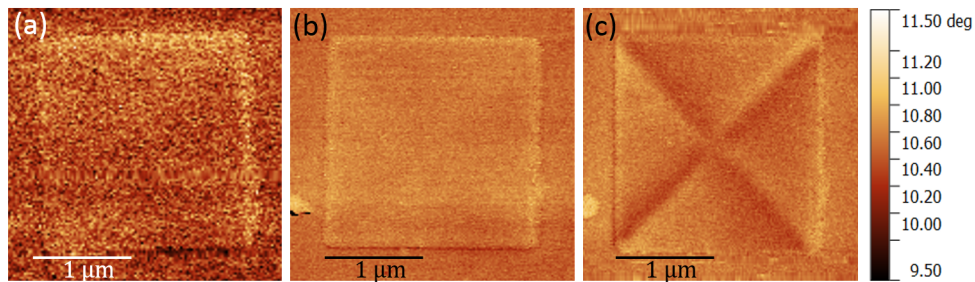


Figure 3.14: MFM measurements performed on a  $2 \times 2 \mu\text{m}^2$  Permalloy square to image the out of plane component  $M_z$ . In all the cases the lift height is 35 nm. In (a) old probes (PPP-LM-MFMR) were used; in (b) and (c) new probes (MESP-LM-V2) were used. In (b) there is no magnetic contrast due to a possible misalignment of the tip. In (c) the Landau configuration is evident.

# Chapter 4

## Results

### 4.1 Micromagnetic simulations

In this section, a hybrid magnetostrictive FM/PE multilayer is simulated with OOMMF. The ferromagnetic component consists of a  $2\ \mu\text{m}$  planar structure. In section § 4.1.1 a Galfenol square is considered and in § 4.1.2 a nickel square is investigated and a few results concerning circular geometries are shown. In the simulations the exchange interaction between the macrospins is included (3.1) as well as the long-ranged demagnetization fields (3.5). In addition to the latter, a strain gradient in the PE is introduced. It is well known (§ 2.5) that the application of a static uniaxial strain to a magnetostrictive material induces an additional uniaxial anisotropy to the magnetic free energy [18]. The uniaxial strain anisotropy (§ 2.1.4) can be written as:

$$U_{me} = K_s \cos^2 \phi \quad (4.1)$$

where  $\phi$  is the angle between the magnetization and the strain, which has been assumed to be along the  $[100]$  direction. Neglecting any small component along  $[010]$ ,  $\epsilon_{yy} = 0$ , the magnetoelastic anisotropy constant is given by the magnetoelastic coefficient  $B_1$  and the normal strain  $\epsilon_{xx}$ :

$$K_s = B_1 \epsilon_{xx} \quad (4.2)$$

$\epsilon_{xx}$  is given by:

$$\epsilon_{xx}(y) = \left( \frac{d\epsilon}{dy} \right) y + \beta \quad (4.3)$$

So that equation (4.1) can be written as:

$$U_{me} = (C + \alpha \cdot y) \cos^2 \phi \quad (4.4)$$

Here,  $\alpha$  is the gradient of the uniaxial anisotropy due to the strain gradient  $d\epsilon/dy$ , and  $C$  is a uniform uniaxial anisotropy coming from the uniform strain  $\beta$ . Thus, the  $x$ -component of the strain is now dependent on the position in  $\hat{y}$  enabling a gradient in the strain. The strain gradient is given by the second term, whereas the first term allows to control the symmetry of the gradient. For example, setting  $C = 0$  allows an antisymmetric strain such that  $K_s(y) = -K_s(-y)$ . For a non-zero  $C$ , such symmetry does not exist about  $y = 0$ . In [16] Ostler et al. already showed that core translations can be achieved introducing a strain induced anisotropy gradient of the form  $\epsilon(y) = (d\epsilon/dy)y$ . In this section we investigate the effect of the strain gradient symmetry on such displacement of the vortex core.

#### 4.1.1 Effects of an anisotropy gradient on a Galfenol element

At equilibrium, without any magnetoelastic anisotropy, the vortex core resides in the centre of the film  $(x,y)=(0,0)$  displaying the Landau flux-closure in Fig.4.1 (a). The vortex core is the small central region with a large  $M_z$  indicating a positive polarity.

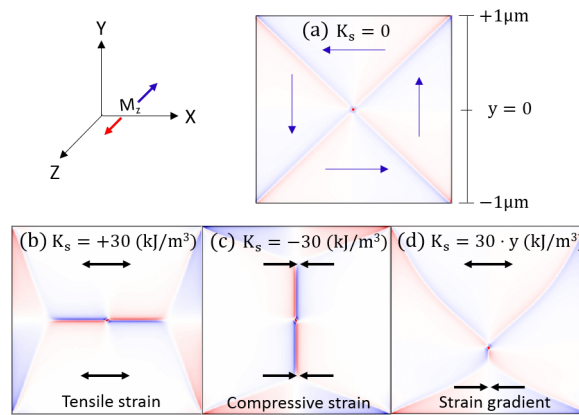


Figure 4.1: The  $z$  component of magnetization of a  $2\ \mu\text{m} \times 2\ \mu\text{m}$   $\text{Fe}_{81}\text{Ga}_{19}$  square when: (a) there is no strain induced anisotropy; when a tensile (b) and compressive (c) spatially uniform uniaxial anisotropy of  $|K_s| = 30\ \text{kJ/m}^3$  is included; and (d) when a uniaxial anisotropy gradient of  $\alpha = 30 \times 10^6\ \text{kJ/m}^4$  is included. The colours represent the magnetization in the positive (red) and negative (blue)  $z$ -direction.

The anti-clockwise sense of the in-plane magnetization is illustrated by the blue arrows which represent the direction of the magnetization in each domain. The four domains are clearly defined by the weaker out of plane magnetization at each domain wall.

If a spatially uniform strain is acting on the heterostructure,  $d\epsilon/dy = 0$  and hence  $\alpha = 0$ , the resulting magnetic configuration is illustrated in Fig.4.1 (b) for a tensile strain ( $\beta > 0$ ) and in Fig.4.1 (c) for a compressive strain ( $\beta < 0$ ), which induces a uniaxial anisotropy of  $K_s = +|C|$  and  $K_s = -|C|$  respectively.  $|C| = 30\text{kJ/m}^3$  corresponds to a typical experimental strain of  $|\beta| \approx 5 \times 10^{-3}$ . The uniform strain-induced uniaxial anisotropy aligns the magnetization in each domain more strongly along the axis of the anisotropy. From the Poisson relation, the tensile (compressive) strain in  $\hat{x}$  also gives rise to a compressive (tensile) strain in  $\hat{y}$  which results in decreasing the size of the domains whose magnetization is aligned along  $|\hat{y}|$  ( $|\hat{x}|$ ) whilst increasing the domains aligned in the  $|\hat{x}|$  ( $|\hat{y}|$ ) directions. Due to the symmetry of the system, there is no motion of the vortex core as there are equal numbers of spins whose energy is minimized by aligning with the anisotropy direction.

In Fig.4.1 (d) a strain induced anisotropy gradient is introduced,  $\alpha \neq 0$ . Here, in contrast to the previous cases, the vortex core displaces from the centre in the negative  $\hat{y}$  direction. First, antisymmetric gradients were studied,  $\beta = 0$ , by setting  $C$  to 0. Elements were simulated for several gradients, from  $\alpha = 5 \times 10^6\text{kJ/m}^4$  to  $\alpha = 40 \times 10^6\text{kJ/m}^4$  in steps of  $5 \times 10^6\text{kJ/m}^4$ . Fig.4.2 (a) shows three of these simulated  $\text{Fe}_{81}\text{Ga}_{19}$  elements,  $\alpha = 10 \times 10^6\text{kJ/m}^4$ ,  $\alpha = 20 \times 10^6\text{kJ/m}^4$  and  $\alpha = 40 \times 10^6\text{kJ/m}^4$  in comparison to the initial state where there is no strain or in other words, where  $\alpha = 0$  (and  $C = 0$ ).

As shown in Fig.4.2 (b), there is a gradual translation of the vortex core to negative  $y$  values with a maximum displacement of  $y \approx 320\text{ nm}$  at  $\alpha = 40 \times 10^6\text{kJ/m}^4$ . In the process, the distortion of the magnetic domains culminates with the emergence of an additional domain wall along the direction of displacement which bridges the domains aligned along  $|\hat{x}|$ . The location of the vortex core as a function of  $\alpha$  is represented in Fig.4.2 (c). Due to the symmetry of the gradient, the bottom half of the structure is subjected to a compressive strain ( $\rightarrow\leftarrow$ ) in the  $x$ -direction and a subsequent tensile strain ( $\leftarrow\rightarrow$ ) in  $\hat{y}$ , with the net effect of reducing the size of the domain whose magnetization is aligned along  $+\hat{x}$  while enlarging the domains aligned in the  $|\hat{y}|$ -directions. The upper half of the structure experiences the inverse situation, a tensile (compressive) strain in  $\hat{x}$  ( $\hat{y}$ ), which

gives rise to an enlargement of the domain whose magnetization is aligned in  $-\hat{x}$  and a decrease in the domains whose magnetization is directed along  $|\hat{y}|$ . The overall result of this strain gradient is to translate the vortex core in the negative  $y$ -direction away from its equilibrium. Such displacement is independent on the chirality and polarity of the configuration but depends on the sign of the gradient as will be seen later.

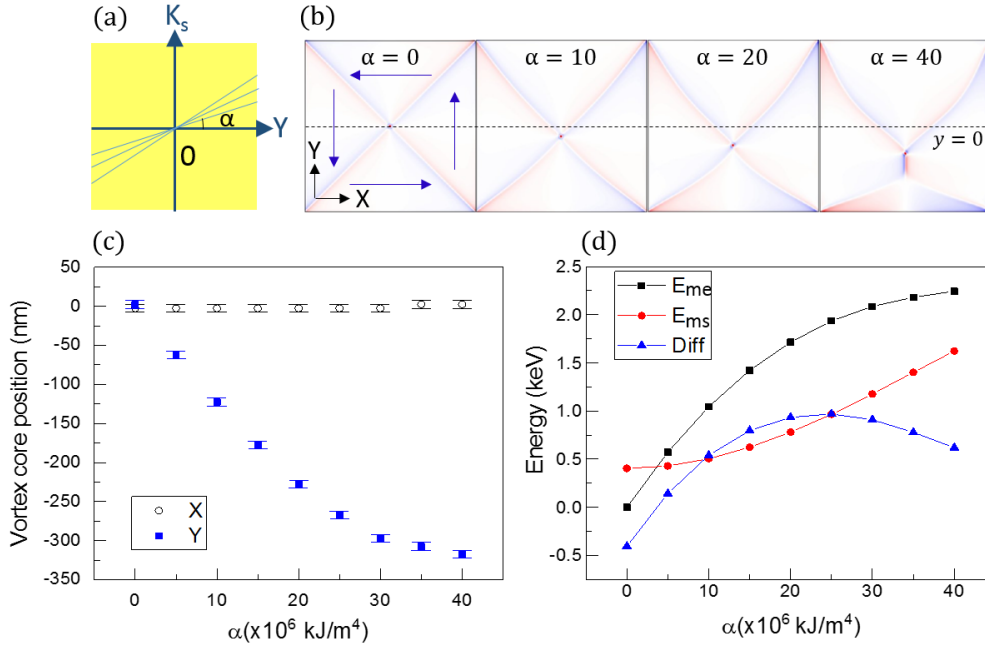


Figure 4.2: (a) Profile of the uniaxial anisotropy,  $K_s$ , for antisymmetric gradients. (b)  $M_z$  of the  $\text{Fe}_{81}\text{Ga}_{19}$  square for several gradients  $\alpha$ . (c) Position of the vortex core as a function of  $\alpha$ . Error bars in this and subsequent graphs in § 4.1 represent the cell size of the grid used in the computation. (d) Magnetoelastic energies,  $E_{me}$  (black squares), magnetostatic energies,  $E_{ms}$  (red circles), and the difference between the two,  $E_{diff} = E_{me} - E_{ms}$  (blue triangles) versus  $\alpha$ .

Although for small gradients the displacement is almost linear in  $\alpha$ , for gradients above  $\alpha = 15 \times 10^6 \text{kJ/m}^4$ , the change in core position with further increases of  $\alpha$  diminishes. This can be understood by looking at the two competing long-ranged free energies, the magnetoelastic energy ( $E_{me}$ ) and the magnetostatic energy ( $E_{ms}$ ). These are shown in Fig.4.2 (d) along with the difference between the two  $E_{diff} = E_{me} - E_{ms}$ . For low values of  $\alpha$ , it is the magnetoelastic energy that increases more rapidly with the amplitude, giving a positive slope in the  $E_{diff}$  curve. However, around  $\alpha = 15 \times 10^6 \text{kJ/m}^4$ , when the core is approximately 230 nm-off centre, the behaviour reverses and the magnetostatic contribution starts increasing more rapidly. That is, the increment in the contribution pushing the core towards the centre becomes bigger than the one pushing the core out of it. As a result, the displacement of the vortex core begins to saturate. At a certain value of  $\alpha$ , when the shape anisotropy starts dominating over the magnetoelastic anisotropy,

the vortex core is expected to reach its maximum displacement possible.

The effects of an additional uniform anisotropy,  $C$ , which acts as an offset to the anisotropy gradient,  $\alpha$ , was also investigated with  $\alpha$  set to  $15 \times 10^6 \text{kJ/m}^4$ , to be within the linear displacement regime as shown previously in Fig.4.2 (c). The offset was varied from  $C = -25 \text{kJ/m}^3$  to  $C = +25 \text{kJ/m}^3$ . To complete the study, the gradient was inverted,  $\alpha = -15 \times 10^6 \text{kJ/m}^4$ . The  $y$  coordinate of the vortex core as a function of  $C$  is represented in Fig.4.3, which includes the zero-offset case ( $C = 0$ ). Blue squares correspond to the systems with  $\alpha = +15 \times 10^6 \text{kJ/m}^4$ , whereas red circles correspond to the systems with a negative gradient  $\alpha = -15 \times 10^6 \text{kJ/m}^4$ .

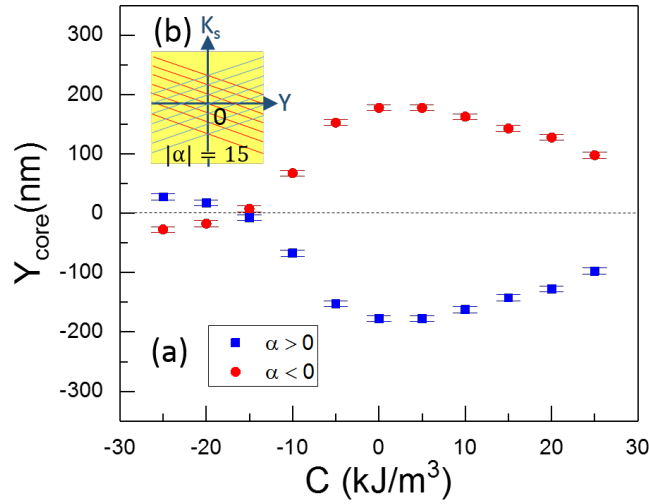


Figure 4.3: (a) Vertical position of the vortex core as a function of  $C$  for the  $2 \mu\text{m} \times 2 \mu\text{m}$   $\text{Fe}_{81}\text{Ga}_{19}$  square for  $\alpha = +15 \times 10^6 \text{kJ/m}^4$  (blue squares) and  $\alpha = -15 \times 10^6 \text{kJ/m}^4$  (red circles). The inset (b) shows the effect of  $C$  on the anisotropy profile.

Once again, the gradient shifts the vortex core along the vertical. As can be observed, the core displacement is maximised,  $|y_{\text{core}}| \approx 200 \text{ nm}$ , when  $C = 0$  so that the strain gradient is antisymmetric about  $y = 0$ . As  $C$  increases towards positive values, the effect of the strain gradient on the core displacement is reduced. For instance, for  $C = 15 \text{kJ/m}^3$  the core displacement is 145 nm compared to 180 nm for  $C = 0$ . Although a reduction of the core displacement occurs for positive values of  $C$ , the shifting is still significant, bigger than 100 nm in all the cases. Especially, the cases where  $C \geq 15 \text{kJ/m}^3$  are particularly relevant to achieve vortex core displacement experimentally. This is because in this range the structure experiences a tensile strain along  $\hat{x}$  over the whole structure, which is easier to fabricate than a gradient going from compressive to tensile.

However, the situation is different for negative offsets,  $C < 0$ . As  $C$  becomes negative, the reduction in the displacement is far greater than for the equivalent positive  $C$ . For  $C = -15\text{kJ/m}^3$  the strain gradient induced core displacement is only 10 nm in the  $y$  direction. Further increases in the magnitude of  $C$  in this direction (more negative) results in the vortex core moving in the opposite  $y$  direction. Such asymmetry regarding the offset can be explained by looking at the domain configurations for  $\alpha = +15 \times 10^6\text{kJ/m}^4$  and  $C \pm 15\text{kJ/m}^3$  in Fig.4.4.

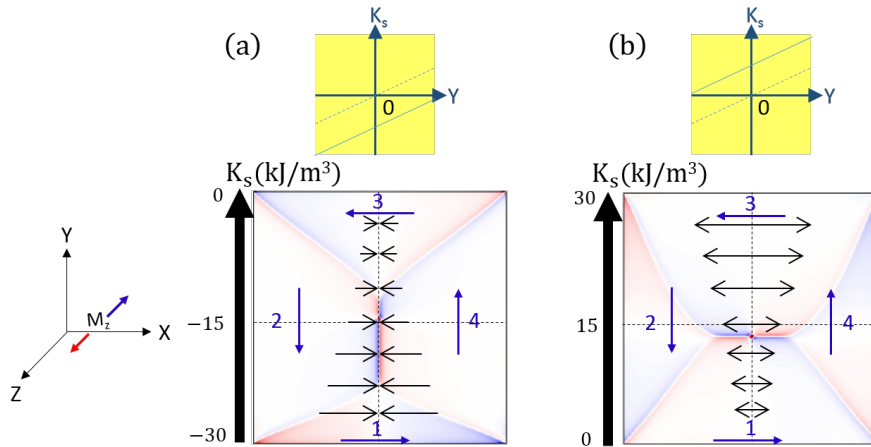


Figure 4.4: Simulated  $\text{Fe}_{81}\text{Ga}_{19}$  squares for (a)  $\alpha = +15 \times 10^6\text{kJ/m}^4$  and  $C = +15\text{kJ/m}^3$  and (b)  $\alpha = +15 \times 10^6\text{kJ/m}^4$  and  $C = -15\text{kJ/m}^3$  showing no symmetry about  $y = 0$ . On top, the corresponding anisotropy profiles are represented.

In the figure above, the profile of the anisotropy gradient is represented on top. The figures on the bottom are once again top views of the simulated squares showing the  $M_z$  component of the magnetization, where numbers 1 to 4 identify the four in-plane domains. The black arrows on the other hand, represent either a tensile strain ( $\leftarrow\rightarrow$ ) or a compressive strain ( $\rightarrow\leftarrow$ ) source of the magnetoelastic energy with  $K_s > 0$  and  $K_s < 0$  respectively. In this context, the arrows represent the value of the anisotropy coefficient throughout the sample, where bigger arrows correspond to bigger magnitudes of  $K_s$ .

Fig.4.4 (a) shows the domain configuration for  $\alpha = +15 \times 10^6\text{kJ/m}^4$  and  $C = +15\text{kJ/m}^3$ . This translates into a strain induced anisotropy going from  $K_s = 0$  at  $y = -1\mu\text{m}$  to  $K_s = -30\text{kJ/m}^3$  at  $y = +1\mu\text{m}$ . The effect of this anisotropy profile is to enlarge the domains 2 and 4 whose magnetization points along the  $|y|$  directions to the extent where they dominate the central region of the structure where the core resides. Domains with magnetization directed along  $|\hat{x}|$  are expelled from this region leaving only a very narrow stripe at the centre of the structure which resembles a Néel domain wall. Thus the strain

induced anisotropy, which is directed in  $\hat{x}$ , has very little effect in this region due to the absence of significant  $M_x$ , the x-component of the magnetization. As a consequence, the vortex displacement is small. However for  $C = -15\text{kJ/m}^3$ , the anisotropy profile enlarges domains 1 and 3 where  $\vec{M}$  is aligned along the tensile strain direction. Domains 2 and 4 are reduced to an extent in the central region that they now resemble a Néel domain wall running in the x-direction. As there is now significant  $M_x$ , in the central region the strain induced anisotropy gradient enlarges domain 1 preferentially to domain 3 (although both increase in area) translating the core in the negative y direction.

The only difference between the elements with  $\alpha > 0$  and  $\alpha < 0$ , is that the vortex core is displaced to opposite directions along  $\hat{y}$ . That is, when the strain gradient is inverted, the displacement of the core is in the positive direction and shows mirror symmetry about  $y=0$  as shown in Fig.4.5.

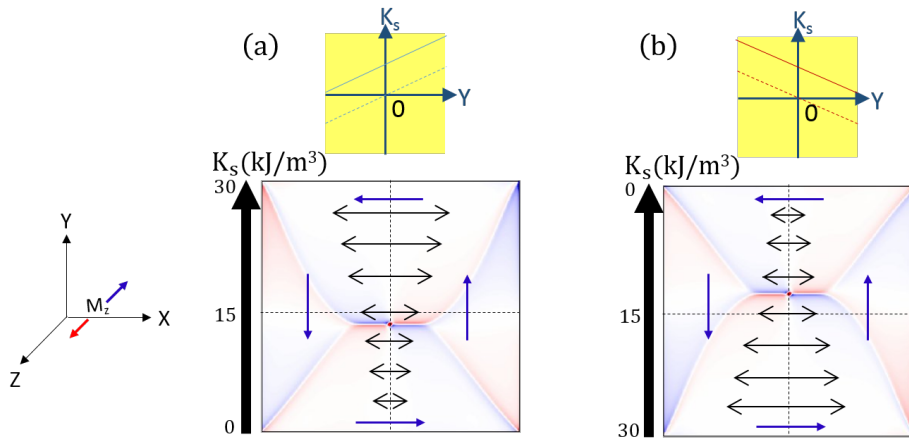


Figure 4.5: Simulated  $\text{Fe}_{81}\text{Ga}_{19}$  squares for (a)  $\alpha = +15 \times 10^6 \text{kJ/m}^4$  and  $C = +15 \text{kJ/m}^3$  and (b)  $\alpha = -15 \times 10^6 \text{kJ/m}^4$  and  $C = +15 \text{kJ/m}^3$  showing symmetry about  $y = 0$ . On top, the corresponding anisotropy profiles are represented.

#### 4.1.2 Effects of an anisotropy gradient on a nickel element

The same study was then carried out for a  $2 \mu\text{m} \times 2 \mu\text{m}$  nickel square by changing the material-specific parameters,  $A$  and  $M_s$ , to those that correspond to pure Ni (Tab.3.1).

For asymmetric gradients, the effect is similar to the one found for the  $\text{Fe}_{81}\text{Ga}_{19}$  element, to displace the vortex core along  $-\hat{y}$  with  $\alpha$ . This is shown in Fig.4.6. On the one hand, the position of the core as a function of the gradient is represented in Fig.4.6 (a). Some of the simulations are also shown in Fig.4.6 (b)-(d). In the latter, it is  $M_x$  that has been colour-represented, as for Ni the out of plane magnetization at the core is too large with

respect to that at the domain walls for these to be observed.

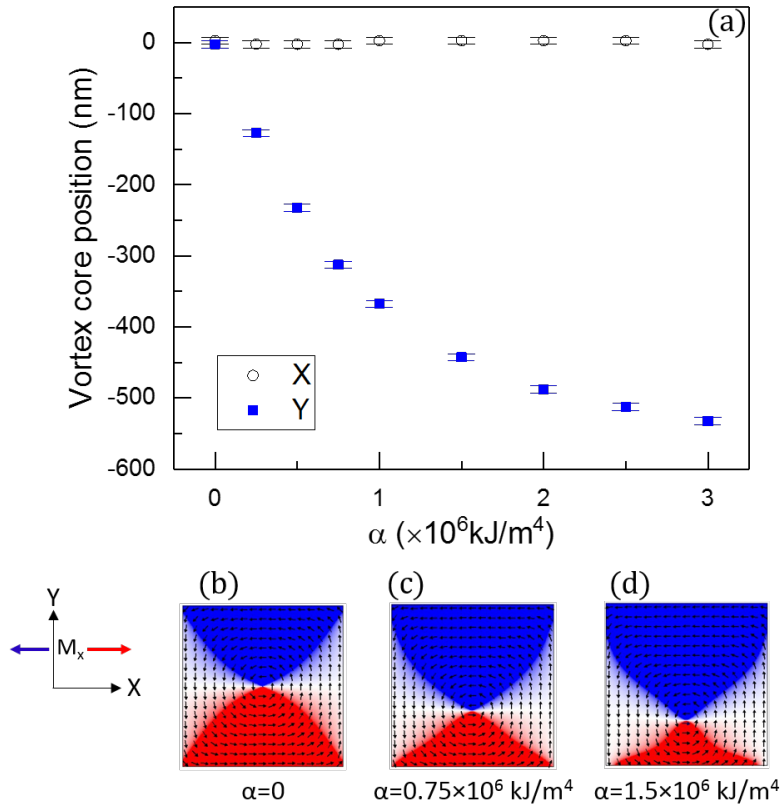


Figure 4.6: (a) Y coordinate of the vortex core as a function of  $\alpha$  for Ni squares with  $C = 0$ . (b), (c) and (d) show the x-component of magnetization for  $\alpha = 0$ ,  $\alpha = 0.75 \times 10^6 \text{kJ/m}^4$  and  $\alpha = 1.5 \times 10^6 \text{kJ/m}^4$  respectively. The black arrows in (b)-(d) represent the direction of the in-plane magnetization.

It must be noted that a positive anisotropy gradient,  $\alpha > 0$ , is now the result of a negative strain gradient,  $d\epsilon/dy < 0$ , as nickel has a negative magnetostriction,  $B_1 \approx -6.2 \text{MJ/m}^3$ . Thus, the vortex core now shifts along the direction of the strain gradient. However, the main difference with respect to Galfenol, is that the effect of the strain-induced anisotropy on the core displacement is significantly bigger in nickel. A usual experimental strain of  $10^{-3}$  corresponds to an anisotropy gradient of  $\alpha \approx 16 \times 10^6 \text{kJ/m}^4$  for  $\text{Fe}_{81}\text{Ga}_{19}$  and  $\alpha \approx 6 \times 10^6 \text{kJ/m}^4$  for Ni. For this value of strain, a displacement of  $|y_{core}| \approx 200 \text{nm}$  is achieved in Galfenol, Fig.4.2 (b), whereas a gradient of  $\alpha = 3 \times 10^6 \text{kJ/m}^4$  is enough to obtain a displacement of  $|y_{core}| > 500 \text{nm}$  for nickel, Fig.4.6 (a). This is due to the fact that Ni has a lower  $M_s$  and thus, the shape anisotropy competing against the magnetoelastic energy is weaker than in  $\text{Fe}_{81}\text{Ga}_{19}$ .

An offset in the strain induced anisotropy,  $C$ , once again plays an important role in the shifting of the core. Fig.4.7 shows the location of the core as a function of  $C$  for a gradient

$$|\alpha| = 1.5 \times 10^6 \text{kJ/m}^4.$$

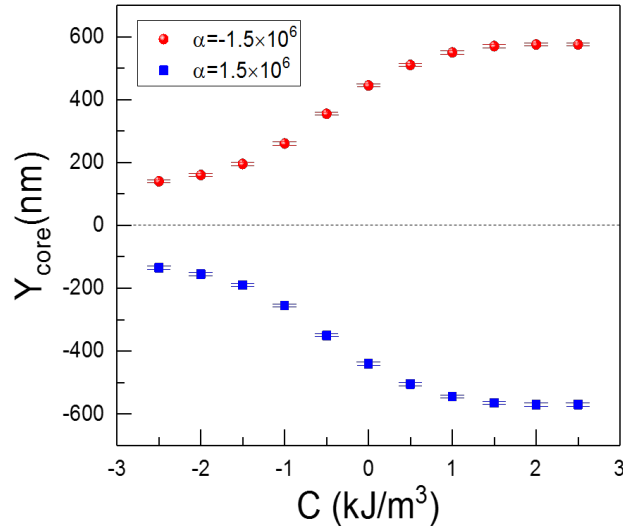


Figure 4.7: Position of the vortex core as a function of  $C$  for the simulated  $2 \mu\text{m}$  Ni squares with  $\alpha = +1.5 \times 10^6 \text{kJ/m}^4$  (blue squares) and  $\alpha = -1.5 \times 10^6 \text{kJ/m}^4$  (red dots).

The symmetry about  $y = 0$  is observed once again when the gradient is reversed. However, the behaviour of the core displacement with  $C$  is different from the one seen in Fig.4.3. While negative values of  $C$  reduce the strain-induced displacement, positive offsets now help to increase it. For instance, for  $C = 1.5 \text{kJ/m}^3$  a shifting of  $\approx 500 \text{nm}$  is observed in comparison to the  $\approx 400 \text{nm}$ -displacement that occurs in the asymmetric case,  $C = 0$ . Indeed, for  $C = 1.5 \text{kJ/m}^3$ , Fig.4.8, the increasing compressive strain in  $+\hat{y}$  enlarges the domain whose magnetization points along  $-\hat{x}$  to such an extent that the core is pushed even more to the bottom edge of the square.

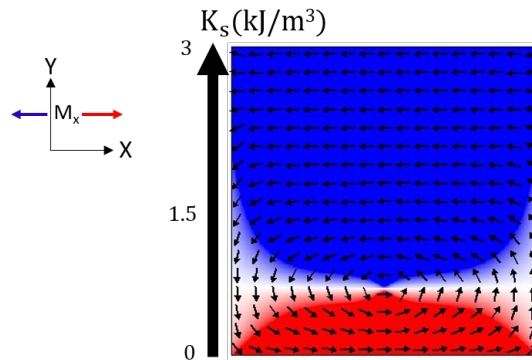


Figure 4.8: Simulated  $2 \times 2 \mu\text{m}^2$  Ni square for  $\alpha = +1.5 \times 10^6 \text{kJ/m}^4$  and  $C = +1.5 \text{kJ/m}^3$ .

Therefore, a non-symmetric strain is in this case favourable to achieve a bigger translation of the core if it leads to a less compressed structure,  $C > 0$ . This way,

when a tensile strain along  $\hat{x}$  is acting over the whole element,  $C > 1.5\text{kJ/m}^3$ , the core displacement along the vertical is maximized,  $|y_{core}| \approx 570\text{ nm}$ . If the strain acting in the Ni element is on average compressive,  $C < 0$ , the core displacement is reduced, but even for  $C = -3\text{kJ/m}^3$  the displacement is still bigger than 100 nm. Thus, the results show that vortex core displacement is easier to achieve in the Ni square than in the Galfenol square.

Given the nice results found for the  $2\text{ }\mu\text{m}$  Ni and  $\text{Fe}_{81}\text{Ga}_{19}$  squares, a preliminary analysis of some other structures was made, which included circular geometries. Fig.4.9 (a) shows the vertical position of the vortex core in a  $2\text{ }\mu\text{m}$  Ni disc as a function of the gradient  $\alpha$  applied to the structure. The behaviour looks similar to that of the Ni square, although a smaller core displacement is achieved for the same value of the gradient. Fig.4.9 (b) and Fig.4.9 (c) show the magnetic configuration of the element when there is no strain applied,  $\alpha = 0$ , and when an antisymmetric gradient of  $\alpha = 3 \times 10^6\text{kJ/m}^4$  is acting on it respectively. The out of plane magnetization is colour-represented revealing the vortex core in red, and the in-plane magnetization is represented by the black arrows which show the in-plane anticlockwise flux. As can be seen, when a strain gradient is applied, the  $M_x$  component is increased in more than half the upper part of the disc while the  $M_y$  component is increased in the very bottom. This results in a vortex core displacement of  $\approx 350\text{ nm}$  along  $-\hat{y}$ . More computations and further analysis will be performed for this geometry but the results so far look promising for inducing vortex core translation on this element as well.

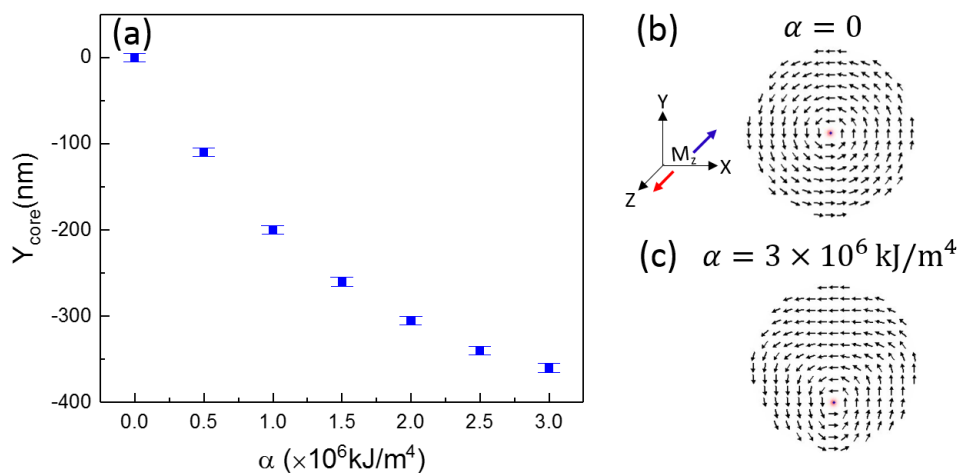


Figure 4.9: (a) Vertical position of the vortex core as a function of the gradient  $\alpha$  ( $C = 0$ ) for the  $2\text{ }\mu\text{m}$  Ni discs.  $M_z$  is shown for (b)  $\alpha = 0$  and (c)  $\alpha = +3 \times 10^6\text{kJ/m}^4$ .

## 4.2 Experimental results

### 4.2.1 Experiment E1

At DLS the devices in E1, Fig.3.2 (a), were investigated. The sample consisted of many Ni devices arranged in 4 rectangular areas in order to study the role of shape anisotropy on the ability to displace vortex cores with strain. The sample is shown in Fig.4.10. Each area is delimited by two large rectangles and contains a set of squares and discs of different sizes. The two geometries are interleaved in columns of different dose, and they increase in size as one goes down along the column. In addition, the mean dose of the set changes in each of the 4 areas. This way, a range of sizes that develop properly are ensured. The smallest devices ( $<1.5 \mu\text{m}$ ) did not come out at all due to issues with the e-beam exposure not being optimal. Also, not all the resist could be removed during the lift-off procedure, affecting the quality of several devices. Despite those issues, a number of good-quality Ni elements between  $2 \mu\text{m}$  and  $6 \mu\text{m}$  were fabricated.

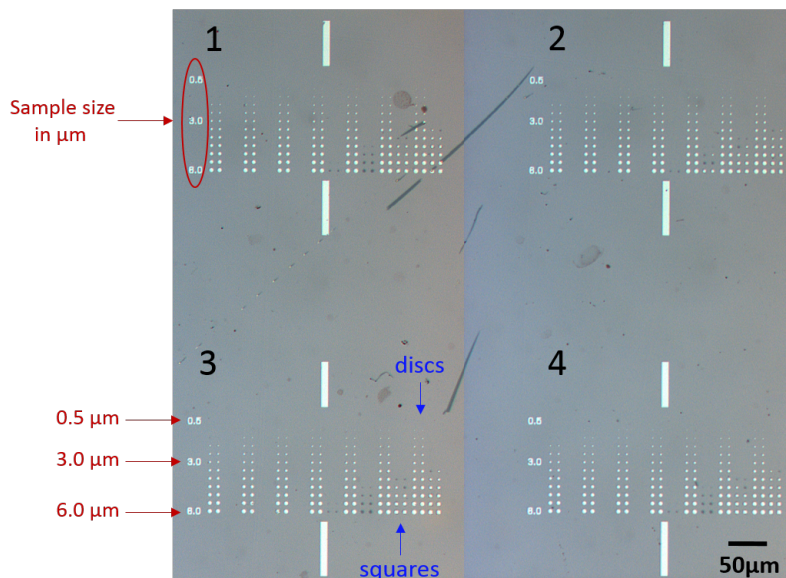


Figure 4.10: Micrograph of the Ni devices in E1 at the four regions 1-4.

Before loading the sample into the PEEM, the electric contact between the two Au electrodes was checked. Any shorts between top and bottom were checked by measuring a capacitance of 2 nF and an infinite resistance between the contacts. A ferroelectric characterization of the PMN-PT was also performed by measuring the polarization while a sinusoidal electric field was applied to the substrate using a *Radiant* ferroelectric tester, as depicted in Fig.4.11 (a). In agreement with Fig.2.8 (b), the polarization showed a 2-

stage reversal hysteresis with the amplitude of the field as shown in Fig.4.11 (b). The ferroelectric hysteresis is characterized by a large saturation and remanent polarization of  $P_s \approx 10.5 \mu\text{C}/\text{cm}^2$  and  $P_r \approx 9.7 \mu\text{C}/\text{cm}^2$  respectively. A coercive field of  $E_c \approx 3.6 \text{kV}/\text{cm}$  is observed, which corresponds to an electric voltage of  $V_c \approx 100 \text{V}$ .

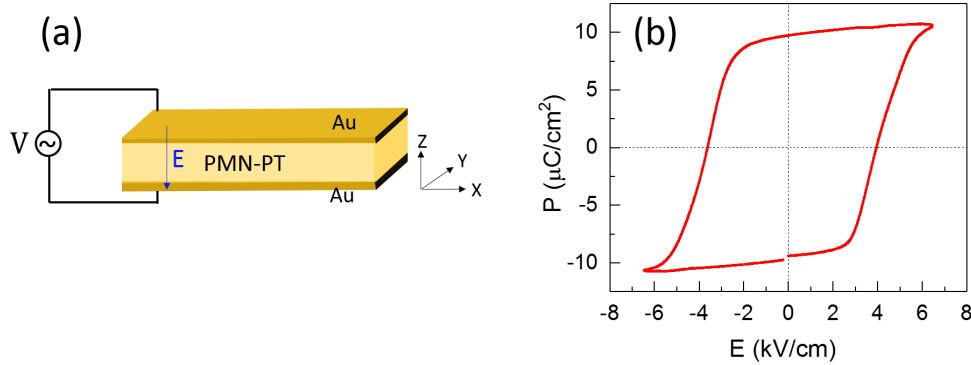


Figure 4.11: (a) Sketch of the PMN-PT substrate under a sinusoidal electric field applied along  $\hat{z}$ ; (b) P-E hysteresis loop measured with the ferroelectric tester.

Once the sample was loaded, a XAS scan was performed in order to search for the  $L_3$  peak of nickel. Fig.4.12 (a) shows the X-ray absorption spectrum measured at two different magnetic regions within the same device. The device is shown in Fig.4.12 (b) and it is in a 2 anti-parallel domain state.

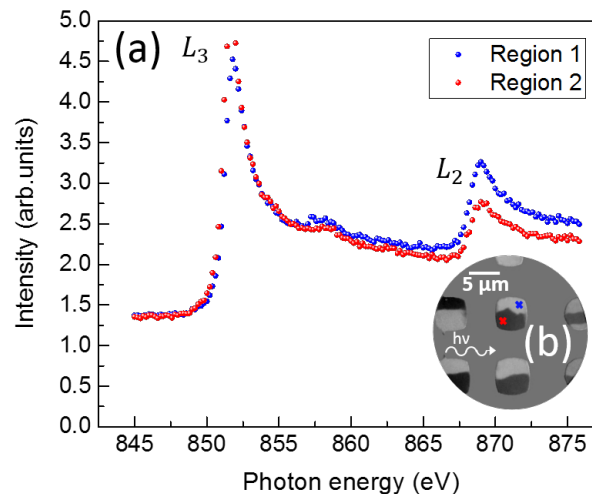


Figure 4.12: (a) X-Ray absorption spectra at two different magnetic regions of the same device showing the difference in intensity at the  $L_3$  and  $L_2$  peaks. In the inset (b), the XMCD image shows the magnetic configuration of the device which consists in two anti-parallel domains. The blue (red) cross points the location where the blue (red) dots were measured.

The blue and red cross indicate the regions at which each spectrum, blue and red dots respectively, was obtained. The photons are left handed circularly polarized in both

cases. In the scanned energy range, both  $L_3$  and  $L_2$  peaks can be observed at the expected energies of  $\approx 851.5\text{eV}$  and  $\approx 870\text{eV}$  respectively. The difference between the two spectra, XMCD, reveals the magnetization-sensitive nature of this measurement (§ 3.3.2.1). The  $L_3$  peak corresponding to the magnetic domain with the red cross has a higher intensity compared to that of the domain with the blue cross, as in these regions the magnetization is in opposite directions (3.7). As a result, the XMCD-PEEM image<sup>1</sup> in the inset shows the first domain, whose magnetization aligns opposite to the direction of the photons, in black and the second domain, whose magnetization points along the direction of the photons, in white.

As Fig. 4.12 (b) reveals, not every device was in a flux closure state after the demagnetization routine in § 3.3.1.3 was carried out. Thus, flux closure configurations had to be found first. In Fig.4.13 (a), a  $4.5\ \mu\text{m}$  disc where magnetization curls in plane can be observed. The direction of the magnetization is represented by the orange arrows. Fig.4.13 (a)-(f) show XMCD-PEEM images of the device when a voltage  $V$  is applied across the PMN-PT. These images are shown together with the ferroelectric loop of the substrate as a function of the voltage.

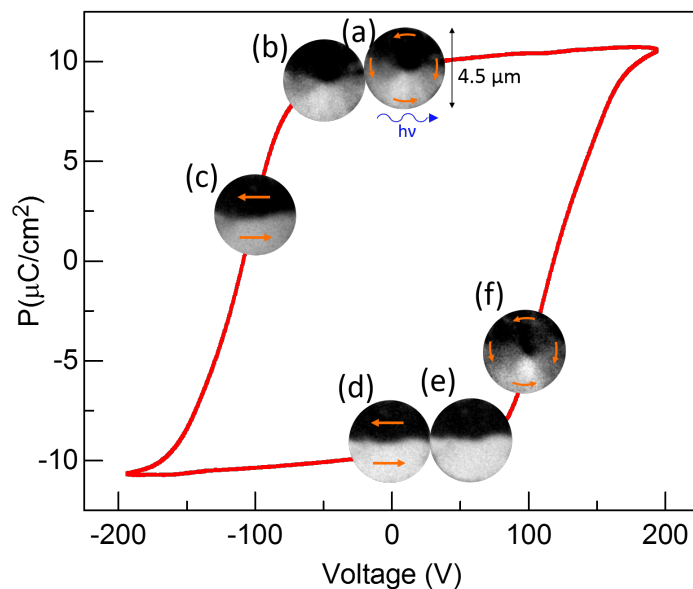


Figure 4.13: PEEM-XMCD images showing the evolution of the in-plane magnetization of a  $4.5\ \mu\text{m}$  circular device in response to the electric voltage applied across the sample: (a) 0V, (b) -50V, (c) -100V; (d) 0V, (e) 50V and (f) 100V. The P-V loop of the PMN-PT is shown in the background.

<sup>1</sup>The XMCD images were obtained by processing the individual PEEM images with *IGOR Pro* according to (3.7) and analysed with *ImageJ*.

First, negative voltages were applied. The voltage was increased in steps of  $|10|$  Volts until  $-150\text{V}$  were reached. Throughout the sweep no evident changes were observed until a voltage of  $\approx -100\text{V}$  was applied, Fig.4.13 (c). At this point, the magnetization that was pointing perpendicular to the direction of the light, which appeared in grey in the XMCD-PEEM image, realigns parallel and anti-parallel to the direction of photons, in white and black respectively. As a result, the flux closure is lost and the magnetic configuration turns into a 2-domain state. The voltage was then swept back to  $0\text{V}$  and reversed to positive values. The two-domain state prevails until the flux closure configuration is retrieved at  $100\text{V}$ , Fig.4.13 (f). That is, near the coercive field,  $V_c$ , magnetization switches between a flux closure state and a two-domain state. This is consistent with a strain-induced switching at the voltages where polarization reversal of the PMN-PT leads to an in-plane strain in the structure.

Several other elements were found in the flux-closure state relevant to this study. Fig.4.14 (a) shows a  $4.5\mu\text{m}$  square displaying 4 in-plane domains whose magnetization aligns along the directions indicated once again by the orange arrows. Fig.4.14 (b) shows a  $4.5\mu\text{m}$  disc where the magnetization curls in-plane in an anti-clockwise sense. The PEEM does not allow for the resolution of the small vortex core whose diameter can be smaller than  $20\text{nm}$ . However, as in these two geometries the exchange induced instability of the flux-closure configuration requires the formation of a vortex core, the presence of the latter is assumed. The bowed domain boundaries in the square in Fig.4.14 (a) seem to correspond very well to the domain walls revealed by the micromagnetic simulations in Fig.4.6 (c). This could be indicative of a remanent strain gradient acting on the elements. The same applies for the disc in Fig.4.14 (b).

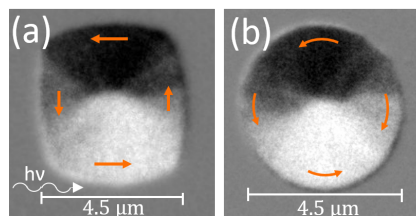


Figure 4.14: XMCD-PEEM images of devices showing bowed domain walls in a flux closure state. Orange arrows represent the direction of the magnetization.

A  $5\mu\text{m}$  square showed a similar 4-domain magnetic configuration when a voltage of  $100\text{V}$  was being applied across the substrate, Fig.4.15 (a). As can be observed, the domains pointing along  $\pm\hat{x}$  are larger than the ones pointing along  $\pm\hat{y}$ , which suggests

that a strain along  $\hat{x}$  is acting on the structure (see Fig.4.1(b)). When the voltage was further increased, there was a modification of the domain pattern. From Fig.4.15 (a) to Fig.4.15 (f) the domain in white, whose magnetization points along  $+\hat{x}$  is enlarged by about 1.58% at the expense of a decrease of the domain in black aligned along  $-\hat{x}$ . At the same time, a small x-component develops at the top left of the element. If the displacement of the vortex core (expected at the union of the 4 in-plane domains) respect to the 100V case is plotted, Fig.4.16, the result is a translation of the core of  $\approx 345$  nm along the vertical. As the magnetic domains do not join in a perfect single point, there is some uncertainty when locating the vortex core within the square. However, the trend of the core moving up along  $\hat{y}$  is clear.

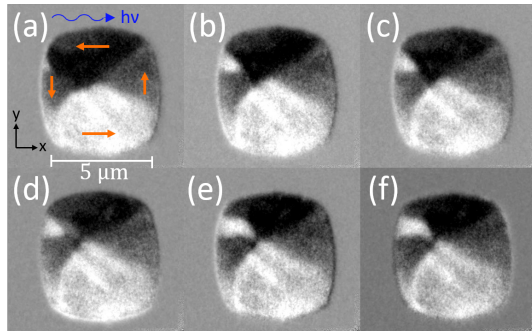


Figure 4.15: PEEM-XMCD images of a  $5\ \mu\text{m}$  square for (a) 100V, (b) 120 V, (c) 140 V, (d) 160 V, (e) 180 V, and (f) 200V.

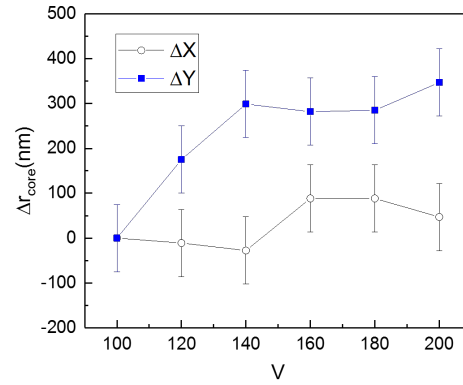


Figure 4.16: Displacement  $r_{core}(V) - r_{core}(100V)$  along  $\hat{x}$  (black circles) and  $\hat{y}$  (blue squares) of the vortex core as a function of the voltage applied across the PMN-PT. The error bars represent a radius of 5 pixels around the location of the core.

This behaviour resembles the displacement of the core studied with OOMMF in § 4.1.2 but with the core moving in the opposite direction, suggesting a strain gradient along  $-\hat{y}$ . However, as the gradient arises from the complex ferroelastic structure of the PMN-PT, the profile of the strain is probably more complicated than the one implemented with OOMMF and a thorough study on the ferroelectric domain configuration is needed to quantify it.

#### 4.2.2 Experiments E2 and E3

To look at the  $2\ \mu\text{m}$  squares in E2 and E3, magnetic force microscopy (§ 3.3.2.3) measurements were performed. The main difference between MFM and PEEM-XMCD is that the first one is sensitive to the out of plane component of magnetization,  $M_z$ ,

whereas PEEM in grazing angle geometry is sensitive to  $M_x$  and  $M_y$ . Thus, MFM enables the imaging of the domain walls and ideally the vortex core in the structures under study. What is more, MFM has a better resolution than the XMCD-PEEM technique which eases the observation of the small vortex core shifts that the micromagnetic simulations have predicted (§ 4.1.1). The idea is to image the magnetostrictive elements in the Landau configuration and measure the effects of the strain gradient generated in the PMN-PT when a voltage is applied through the Au electrodes as represented in Fig.3.2 (E2) and Fig.3.2 (E3). There has not been enough time to perform this study yet, but the steps realized so far towards this goal will be shown in this section.

The squares shown here are  $\text{Fe}_{81}\text{Ga}_{19}$ . Even if the simulations showed that Galfenol elements are less affected by a strain induced anisotropy gradient, see Fig.4.2 (c) and Fig.4.6 (a), they are easier to image with the MFM in comparison to Ni. Indeed,  $\text{Fe}_{81}\text{Ga}_{19}$  has a larger  $M_s$  (Table 3.1) which results in a bigger  $M_z$  in the device, as shown by the OOMMF simulations which displayed a  $M_z$  at the core of the order of  $1 \times 10^6 \text{A/m}$  for  $\text{Fe}_{81}\text{Ga}_{19}$  and  $2 \times 10^5 \text{A/m}$  for Ni. Also, as  $M_s(\text{Fe}_{81}\text{Ga}_{19}) > M_s(\text{Ni})$ , the demagnetization energy (2.17) in Galfenol is larger and it is easier for these structures to form flux closure states in the first place.

AFM images of the Au arms facing the  $2 \mu\text{m}$   $\text{Fe}_{81}\text{Ga}_{19}$  square are shown in Fig.4.17 (a) and Fig.4.17 (c) for E2 and E3 respectively. This and the rest of AFM/MFM images that will be shown in this section have been processed with the software *Gwyddion*. Among other corrections, faulty lines have been removed and the data have been properly levelled. The topography measurements reveal electrodes with a thickness of around 150-200 nm and approximately 40 nm-thick squares. The main distances extracted from the AFM measurements are indicated in light grey. Figures 4.17 (b) and 4.17 (d) show the profile of the scan line that crosses the centre of the  $\text{Fe}_{81}\text{Ga}_{19}$  element in Fig.4.17 (a) and Fig.4.17 (c) respectively. The white feature at the bottom of the square in Fig.4.17 (c) reveals a very high edge which indicates the presence of PMMA under the ferromagnetic layer that was not removed during the lithography process. This effect was reduced by soaking the sample in ACE again.

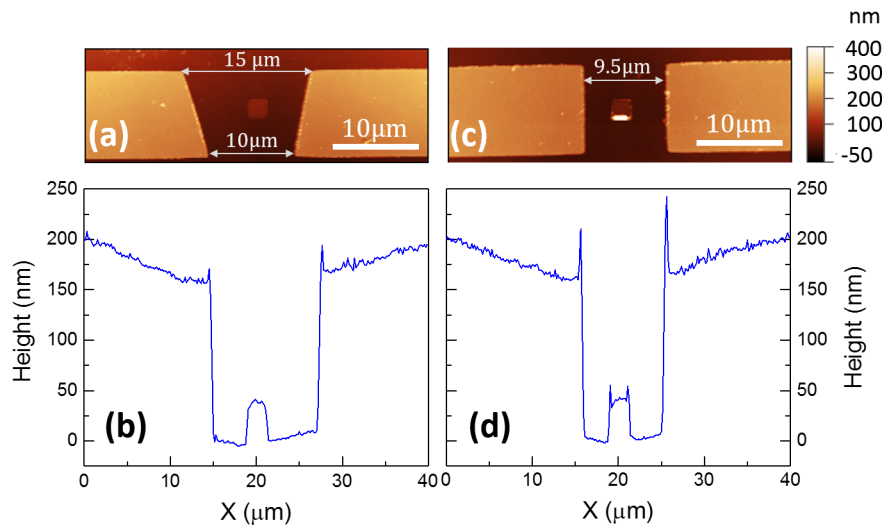


Figure 4.17: (a) and (c) are topography images of the  $\text{Fe}_{81}\text{Ga}_{19}$  elements between the Au electrodes in E2 and E3 respectively. (b) and (d) are profiles of the scan line crossing the centre of the element in (a) and (c) respectively.

Fig.4.18 (a) shows the topography of the square in E3 prior to the additional soaking. Here, the presence of the PMMA extends beyond the bottom edge of the square and includes part of the left edge and the right edge of the device. Fig.4.18 (b) shows the magnetic contrast as measured by MFM. As can be observed, the tall edges, in addition to making surface mapping more difficult, prevent the measurement of the magnetic forces in a wide area given that the phase difference for the magnetic signal  $\Delta\phi_{mag} \approx 0.3^\circ$  is lower than that arising from the resist,  $\Delta\phi_{resist} \approx 0.45^\circ$ . This makes the interpretation of the magnetic properties of the square difficult.

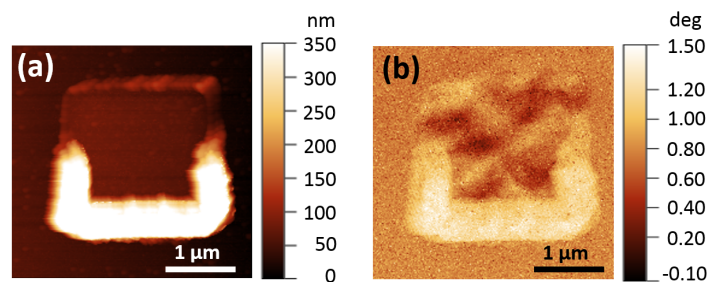


Figure 4.18: (a) topography and (b) magnetic contrast of the  $\text{Fe}_{81}\text{Ga}_{19}$  element in E3 before soaking the sample in ACE.

The topography of the Galfenol elements after the extra cleaning is shown in Fig.4.19 (a) and Fig.4.19 (c) for E2 and E3 respectively. The mean height of the structures is  $39 \pm 2$  nm and  $42 \pm 2$  nm respectively. Comparing Fig.4.18 (a) with Fig.4.19 (c), the improvement achieved with the ACE can be observed. The left and right edges of the element are now

sharper, although some resist still remains especially in the bottom edge. Fig.4.19 (b) and Fig.4.19 (d) are the corresponding magnetic contrast images showing the  $M_z$  component of the squares in E2 and E3.

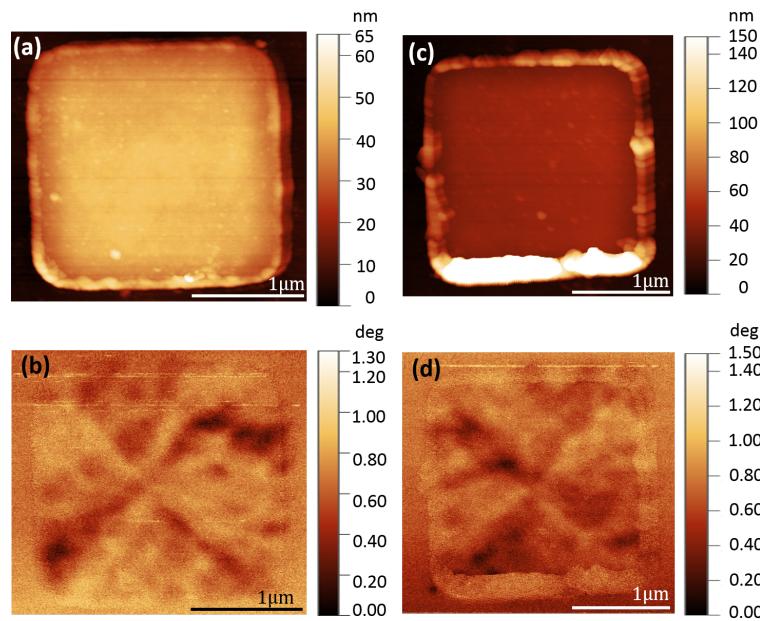


Figure 4.19: (a) and (b) show the topography of the  $\text{Fe}_{81}\text{Ga}_{19}$  elements in E2 and E3 respectively. (c) and (d) show the magnetic contrast in the squares in E2 and E3 respectively.

Both elements show what seems to be a Landau flux closure similar to Fig.4.1 (a). However, this time, the domain walls could not be resolved as neatly as in the Permalloy element that had been previously measured as a test, Fig.3.14 (c). The magnetic contrast in Fig.4.19 (b) and Fig.4.19 (d) appears blurry and the domain walls cannot be resolved well. This effect is probably due to the roughness of the surface. Fig.4.20 (a) and Fig.4.20 (b) are 3D images of one of the  $\text{Fe}_{81}\text{Ga}_{19}$  squares and the Permalloy element respectively. With *NanoScope Analysis* the average roughness,  $R_a$ , and the root mean square roughness,  $R_q$ , of the data within the box defined by the dashed lines were calculated.

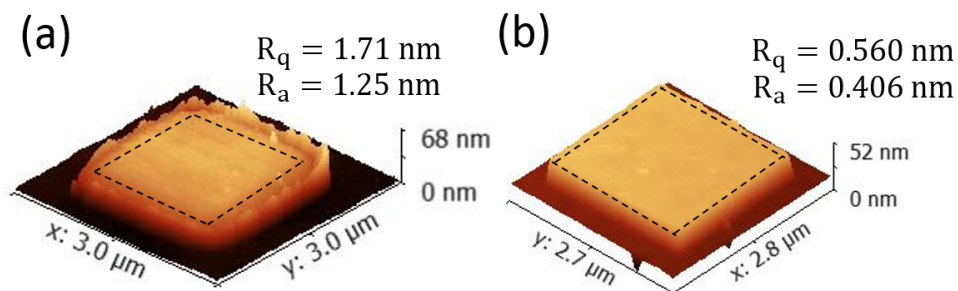


Figure 4.20: 3D images of (a) the  $\text{Fe}_{81}\text{Ga}_{19}$  square in E2 and (b) the Permalloy element in the waveguide used previously as a test sample, Fig.3.13.

According to the results, which are indicated in the figure, the  $\text{Fe}_{81}\text{Ga}_{19}$  element is rougher. Such height variations can affect the magnetic measurement given that the magnetic signal is only of around  $0.32^\circ$ . This effect was not observed with the PEEM because this technique is sensitive to the in-plane component rather than the one perpendicular to the sample. The roughness of the  $\text{Fe}_{81}\text{Ga}_{19}$  elements probably arises from the substrate and has ultimately been transferred to the ferromagnetic devices on top.

The following step will be making the connections between the electrodes in order to apply a voltage to the structure. However, because small displacements of the vortex core (at the crossing point) are being sought, smoother samples might be needed to precisely locate the vortex core within the element.

## Chapter 5

# Conclusions and outlook

In the present work, the effects of a strain induced anisotropy gradient in Ni and Fe<sub>89</sub>Ga<sub>19</sub> thin-film elements displaying a flux-closure vortex state have been investigated. For the elements, both square and circular geometries have been considered.

First, 2 μm Ni and Fe<sub>89</sub>Ga<sub>19</sub> elements have been simulated using OOMMF. A strain gradient has been simulated by introducing a uniaxial anisotropy gradient arising from the magnetoelastic energy. The micromagnetic simulations have shown that, unlike spatially uniform strains [18], antisymmetric strain gradients induce vortex core shifts of hundreds of nanometres. The translation of the core occurs along the direction of the gradient and increases with the latter until the magnetostatic energy starts dominating over the magnetoelastic contribution. For nickel, core translations bigger than 500 nm have been observed. The effect is smaller for the Fe<sub>81</sub>Ga<sub>19</sub> element, but large displacements of around 320 nm can still be achieved. Finally, non-symmetric strains have also been studied by the introduction of an offset,  $C$ , to the anisotropy gradient. Such an offset can affect significantly the core displacement depending on the structure. In nickel, the offset can both increase or reduce core displacement. In Galfenol, the effect of the offset is detrimental and can reduce the displacement to such an extent that there is almost no motion of the vortex core.

Then, three experiments were designed to induce an anisotropy gradient to a ferromagnetic element. The architecture of the device is always a magnetoelectric heterostructure, wherein electric fields applied to a piezoelectric substrate generate magnetoelastic anisotropy in the element via magnetostriction effects. In order to generate the gradient, the first experiment (E1) exploits the ferroelastic multi-domain

configuration of a PMN-PT substrate. A PMN-PT substrate was sandwiched between two Au contacts and an electric voltage was applied between the two while XMCD-PEEM measurements were performed. The domain configuration of the Ni elements changes as an electric voltage is applied. The changes observed for one of the nickel squares displaying a Landau flux closure indicate translation of the vortex core. However, a thorough study of the ferroelastic domain configuration of the PMN-PT is still needed to gain information about the strain acting on the structure. One of the approaches that is being considered is to image the ferroelectric domains via piezoresponse force microscopy (PFM).

The second and third experiments (E2 and E3), create a strain gradient between two metallic electrodes patterned on top of the PMN-PT in a similar way to [32], where a  $\text{Fe}_{81}\text{Ga}_{19}$  element is located. MFM measurements were performed in this case to track the position of the vortex core. Magnetic contrast seems to point to a Landau configuration which would mean the presence of a vortex core at the union of the domain walls. However, the domain walls could not be resolved very well possibly due to the roughness of the surface, making it difficult to precisely locate the vortex core within the element. Unfortunately, there has been no time to study the application of an electric voltage to the structure. The idea is to use indium wire to make the contact between the electrodes and measure any changes on the magnetic configuration with the MFM. The strain would be quantified by measuring the stretching of the ferromagnetic elements. Experiments E2 and E3 are particularly exciting because unlike E1 they would provide full control on the strain gradient and hence, on the translation of the vortex core. This opens the possibility for a low energy mechanism to excite vortex core dynamics.

# Bibliography

- [1] S. Seki, X. Z. Yu, S. Ishiwata, and Y. Tokura, *Science*, vol. 336, no. 198, 2012.
- [2] K. Guslienko, *J Nanosci Nanotechnol.*, vol. 8, no. 6, pp. 2745–60, 2008.
- [3] N. Kikuchi, S. Okamoto, O. Kitakami, Y. Shimada, S. G. Kim, Y. Otani, and K. Fukamichi, *J. Appl. Phys.*, vol. 90, no. 6548, 2001.
- [4] R. P. Cowburn, D. K. Koltsov, A. O. Adeyeye, M. E. Welland, and D. M. Tricker, *Phys. Rev. Lett.*, vol. 83, no. 5, 1999.
- [5] A. Thiaville, J. M. García, R. Dittrich, J. Miltat, and T. Schref, *Phys. Rev. B*, vol. 67, no. 094410, 2003.
- [6] R. Hertel, *Nat. Nanotechnol.*, vol. 8, no. 318, 2013.
- [7] V. Uhr, M. Urbanek, L. Hladk, J. Spousta, M.-Y. Im, P. Fischer, N. Eibagi, J. J. Kan, E. E. Fullerton, and T. Sikola, *Nat. Nanotechnol.*, vol. 8, no. 66, 2013.
- [8] Q. F. Xiao, J. Rudge, B. C. Choi, Y. K. Hong, and G. Donohoe, *Appl. Phys. Lett.*, vol. 89, no. 262507, 2006.
- [9] R. Hertel, S. Gliga, M. Fahnle, and C. M. Schneider, *Phys. Rev. Lett.*, vol. 98, no. 117201, 2007.
- [10] M. Weigand, B. V. Waeyenberge, A. Vansteenkiste, M. Curcic, V. Sackmann, H. Stoll, T. Tylliszczak, K. Kaznatcheev, D. Bertwistle, G. Woltersdorf, C. H. Back, and G. Schutz, *Phys. Rev. Lett.*, vol. 102, no. 077201, 2009.
- [11] B. V. Waeyenberge, A. Puzic<sup>1</sup>, H. Stoll, K. W. Chou, T. Tylliszczak, R. Hertel, M. Fahnle, H. Bruck, K. Rott, G. Reiss, I. Neudecker, D. Weiss, C. H. Back, and G. Schutz, *nature*, vol. 444, no. 05240, 2006.

- [12] M. Curcic, B. V. Waeyenberge, A. Vansteenkiste, M. Weigand, V. Sackmann, H. Stoll, M. Fahnle, T. Tylliszczak, G. Woltersdorf, C. H. Back, and G. Schutz, *Phys. Rev. Lett.*, vol. 101, no. 197204, 2008.
- [13] K.-S. Lee and S.-K. Kim, *Phys. Rev. Lett.*, vol. 78, no. 014405, 2008.
- [14] G. de Loubens, A. Riegler, B. Pigeau, F. Lochner, F. Boust, K. Gusliencko, H. Hurdequint, L. Molenkamp, G. Schmidt, A. N. Slavin, V. S. Tiberkevich, N. Vukadinovic, and O. Klein, *Phys. Rev. Lett.*, vol. 102, no. 177602, 2009.
- [15] V. S. Pribiag, I. N. Krivorotov, G. D. Fuchs, P. M. Braganca, O. Ozatay, J. C. Sankey, D. C. Ralph, and R. A. Buhrman, *Nat. Phys.*, vol. 3, no. 498, 2007.
- [16] T. A. Ostler, R. Cuadrado, R. W. Chantrell, A. W. Rushforth, and S. A. Cavill, *Phys. Rev. Lett.*, vol. 115, no. 067202, 2015.
- [17] Q. Mistral, M. van Kampen, G. Hrkac, J.-V. Kim, T. Devolder, P. Crozat, C. Chappert, L. Lagae, and T. Schrefl, *Phys. Rev. Lett.*, vol. 100, no. 257201, 2008.
- [18] D. E. Parkes, R. Beardsley, S. Bowe, P. A. W. I. Isakov, K. W. Edmonds, R. P. Champion, B. L. Gallagher, A. W. Rushforth, and S. A. Cavill, *Appl. Phys. Lett.*, vol. 105, no. 062405, 2014.
- [19] J. L. Hockel, A. Bur, K. P. W. Tao Wu, and G. P. Carman, *Appl. Phys. Lett.*, vol. 100, no. 022401, 2012.
- [20] E. L. L. LANDAU, *Phys. Zeitsch. der Sow.*, vol. 8, no. 153, 1935.
- [21] T. Shinjo, T. Okuno, Hassdorf, K. Shigeto, and Ono, *Science*, vol. 289, no. 931, 2000.
- [22] S. Mamica, "Spin-wave dynamics in the presence of magnetic vortices," in *Vortex Dynamics and Optical Vortices*, H. Perez-de Tejada, Ed. InTech, 2017, ch. 13.
- [23] F. Hoffmann, G. Woltersdorf, K. Perzlmaier, A. N. Slavin, V. S. Tiberkevich, A. Bischof, D. Weiss, and C. H. Back, *Phys. Rev. B*, vol. 76, no. 014416, 2007.
- [24] G. M. Wysin, *Phys. Rev. B*, vol. 54, no. 21, 1996.
- [25] B. A. Ivanov, H. J. Schnitzer, F. G. Mertens, and G. M. Wysin, *Phys. Rev. B*, vol. 58, no. 13, 1998.
- [26] A. A. Thiele, *Phys. Rev. Lett.*, vol. 30, no. 6, 1973.

- [27] D. J. Clarke, O. A. Tretiakov, G.-W. Chern, Y. B. Bazaliy, and O. Tchernyshyov, *Phys. Rev. B*, vol. 78, p. 134412, Oct 2008.
- [28] T. Liu and C. S. Lynch, *Acta Mater.*, vol. 51, no. 407, 2003.
- [29] T. Wu, P. Zhao, M. Bao, A. Bur, J. L. Hockel, K. Wong, K. P. Mohanchandra, C. S. Lynch, and G. P. Carman, *J. Appl. Phys.*, vol. 109, no. 124101, 2011.
- [30] K. Uchino, *Advanced piezoelectric materials*. Woodhead Publishing, 2010.
- [31] R. P. Beardsley, S. Bowe, D. E. Parkes, C. Reardon, K. W. Edmonds, B. L. Gallagher, S. A. Cavill, and A. W. Rushforth, *Sci. Rep.*, vol. 7, no. 7613, 2017.
- [32] J. Cui, J. L. Hockel, P. K. Nordeen, D. M. Pisani, C. yen Liang, G. P. Carman, and C. S. Lynch, *Appl. Phys. Lett*, vol. 103, no. 232905, 2013.
- [33] A. Aharoni, *J. Appl. Phys.*, vol. 83, no. 6, 1998.
- [34] Y. Sato, T. Hirayama, and Y. Ikuhara, *Phys. Rev. Lett.*, vol. 107, no. 187601, 2011.
- [35] M. Buzzi and et al., *Phys. Rev. Lett.*, vol. 111, no. 027204, 2013.
- [36] I. Rafalovskyi, M. Guennou, I. Gregora, and J. Hlinka, *Phys. Rev. B*, vol. 93, no. 064110, 2016.
- [37] I. Rafalovsky, M. Guennou, M. Gregora, and I. Hlinka, *Phys.Rev.B.*, vol. 109, no. 124101, 2011.
- [38] D. Lee, R. K. Behera, P. Wu, H. Xu, Y. L. Li, S. B. Sinnott, W. R. Phillpot, L. Q. Chen, and V. Gopalan, *Phys. Rev. B*, vol. 80, no. 060102, 2009.
- [39] J. Ouyang, D. M. Kim, C. B. Eom, R. Ramesh, and A. L. Roytburd, *Smart Mater. Struct.*, vol. 14, no. 5245282, 2005.
- [40] <http://blog.bruckerfmprobes.com>.